Sara Tamara Mantey

Técnicas Optoelectrónicas de Controlo da Polarização para Tecnologias Quânticas

Electro-Optic Polarization Control Techniques for Quantum Technologies

Universidade de Aveiro
2021

Sara Tamara Mantey

Técnicas Optoelectrónicas de Controlo da Polarização para Tecnologias Quânticas

Electro-Optic Polarization Control Techniques for Quantum Technologies

Dissertação apresentada à Universidade de Aveiro para cumprimento dos requesitos necessários à obtenção do grau de Mestre em Engenharia Física, realizada sob a orientação científica do Doutor Nelson de Jesus Cordeiro Muga, Investigador Auxiliar do Instituto de Telecomunicações, e sob coorientação científica do Doutor Nuno Alexandre Peixoto Silva, Investigador Auxiliar do Instituto de Telecomunicações.

o júri / the jury

presidente / president

Prof.ª Margarida Maria Resende Vieira Facão
Professora Auxiliar do Departamento de Física da Universidade de Aveiro

vogais / examiners committee

Doutor Nelson de Jesus Cordeiro Muga
Investigador Auxiliar do Instituto de Telecomunicações (orientador)

Prof. Doutor Manfred Niehus
Professor Adjunto da Área Departamental de Física do Instituto Superior de Engenharia de Lisboa (ISEL)

agradecimentos / acknowledgements

Em primeiro lugar agradeço aos meus orientadores Nelson Muga e Nuno Silva por toda a orientação, apoio e disponibilidade incansável que mostraram durante toda a realização deste trabalho. Agradeço também a todo o grupo de comunicações óticas pelo apoio prestado, especialmente à Mariana Ramos pela sua disponibilidade e pelas imensas sugestões valiosas, quer durante o desenvolvimento experimental, quer pelo apoio na escrita desta dissertação.

Agradeço à Universidade de Aveiro e toda a sua comunidade. Em particular, agradeço também ao Departamento de Física, incluindo toda a comunidade departamental que acabou por tornar este lugar como uma segunda casa durante os passados 5 anos. Obrigada também ao Instituto de Telecomunicões por ter disponibilizado as condições necessárias à realização da componente experimental deste trabalho, particularmente aos projetos DSPMetroNet (POCI-01-0145-FEDER-029405) QuantumMining (POCI-01-0145-FEDER-031826) e UIDB/50008/2020-UIDP/50008/2020 (actions DigCORE, QuRunner, and QUESTS).

Dedico também um grande obrigada a todos os meus amigos que me apoiaram todos estes anos e que assim tornaram esta etapa da minha vida realizável e muito mais agradável, particularmente àqueles próximos o suficiente para estarem a ler estes agradecimentos.

Agradeço também à minha família, especialmente à minha mãe, Elisabeth, que sempre me apoiou e sem a qual certamente não teria conseguido chegar a este ponto, primeiro porque sem ela não teria nascido e segundo porque nunca parou de acreditar em mim mesmo nos pontos mais baixos da minha vida, nos quais sempre esteve lá para me suportar e ajudar.

Obrigada!

Palavras Chave

comunicações quânticas, codificação na polarização, distribuição quântica de chaves, estado de polarização, flutuação da polarização.

Resumo

A quantidade de informação sensível, desde informação pessoal, financeira, ou médica, até segredos comerciais ou governamentais, que é transmitida através da internet teve um crescimento exponencial nos últimos anos. Este crescimento veio reforçar a necessidade de termos sistemas de encriptação de dados altamente seguros, nomeadamente na camada física dos sistemas. A distribuição de chaves quântica (QKD) foi proposta como solução viável e promissora para manter a segurança dos dados transmitidos, sendo que a segurança de sistemas QKD se deve à implementação de protocolos criptográficos baseados nos princípios da mecânica quântica.

Esta dissertação foca-se no estudo de técnicas de monitorização e controlo eletro-ótico da polarização para ser aplicado em tecnologias quânticas, nomeadamente em sistemas QKD com codificação na polarização. Inicialmente, as flutuações aleatórias da polarização presentes em links de fibras óticas foram modeladas e caracterizadas experimentalmente. A caracterização experimental incorporou medições no laboratório e em campo. As medições em campo foram realizadas em duas localidades diferentes: um anel de fibra ótica na cidade de Aveiro (com um comprimento total de 6.6 km), e um link ótico na cidade de Lisboa (com um comprimento de 3.1 km). Os resultados mostraram que as flutuações da polarização são mais elevadas para as medições feitas em laboratório do que as feitas em campo. De seguida, um algoritmo para a geração automática e determinística de estados de polarização (SOP), com aplicação direta em sistemas QKD com codificação na polarização, foi proposto e validado. O algoritmo de geração de SOPs proposto usa um controlador eletrónico de polarização (EPC), cujos elementos ativos consistem numa concatenação de várias lâminas de atraso baseadas na aplicação de pressão na fibra. De forma a apoiar uma avaliação inicial do algoritmo, realizou-se uma caracterização das lâminas de atraso do EPC. Por fim, a eficiência do algoritmo foi experimentalmente averiguada utilizando um sistema QKD com codificação na polarização. Um Arduino Due foi utilizado para controlar as diferentes lâminas de atraso do EPC e para realizar uma estimação da taxa de bits quânticos errados (QBER) do sistema. O QBER foi medido por períodos de 4 horas e 10 horas, respetivamente, aquando da geração de dois ou quatro SOPs. Considerando ambas as medições, obteve-se um QBER médio de 2%. Os resultados mostram o potencial do método proposto relativamente à geração automática e determinística de SOPs, assim demonstrando viabilidade para a sua implementação prática num sistema QKD com codificação na polarização.

Keywords

polarization-encoding, polarization drift, quantum communications, quantum key distribution, state-of-polarization.

Abstract

The amount of sensible information, ranging from personal, financial or health data to commercial or governmental secrets, that is transmitted through the Internet has shown exponential growth over the past few years. This growth increased the need for highly secure encryption systems, namely at the physical layer. Quantum key distribution (QKD) has been proposed as a viable and promising solution to keep transmitted data safe, with its security relying on the implementation of cryptographic protocols involving the principles of quantum mechanics.

This dissertation focuses on the study of electro-optic polarization monitoring and control techniques to be applied in quantum technologies, namely in polarization-encoding QKD systems. Initially, the random polarization drift present in optical fiber links was modeled and experimentally characterized. The experimental characterization encompassed both laboratory and field measurements, with the latter being carried out in two different sites: an optical loop in the city of Aveiro (with a total fiber length of 6.6 km), and an optical link in the city of Lisbon (with a fiber length of 3.1 km). The results showed a higher polarization drift for the laboratory measurements than for the field measurements. After, an algorithm for the automatic and deterministic state of polarization (SOP) generation with direct application in polarization-encoded QKD systems was proposed and validated. The proposed SOP generation algorithm uses an electronic polarization controller (EPC), whose active elements entail the concatenation of several fiber-squeezing-based waveplates. To support the initial algorithm assessment, a full characterization of the waveplates was carried out. After, the effectiveness of the proposed algorithm was experimentally assessed in a polarization-encoded QKD testbed. An Arduino Due was used to control the different waveplates of the EPC through the estimation of the quantum bit error rate (QBER) of the system. The QBER was measured for periods of 4 hours and 10 hours when generating two and four SOPs, respectively, with an overall average QBER of 2%. Results show the potential of the proposed method regarding the generation of automatic and deterministic SOPs, thus demonstrating viability for its practical implementation in polarization-encoding QKD systems.

Contents

Acronyms

QBER Quantum Bit Error Rate.

ACF Autocorrelation Function.

BB84 Bennett-Brassard 1984.

BS Beam Splitter.

DV Discrete-Variable.

ECL External Cavity Laser.

EPC Electronic Polarization Controller.

HWP Half Waveplate.

LP Linear Polarizer.

MZM Mach-Zehnder Modulator.

OF Optical Filter.

OTDR Optical Time-Domain Reflectometer.

PBS Polarization Beam Splitter.

PC Polarization Controller.

PIN p-i-n Photodiode.

QKD Quantum Key Distribution.

QWP Quarter Waveplate.

SOP State of Polarization.

SPD Single-Photon Detector.

VOA Variable Optical Attenuator.

WDM Wavelength-Division Multiplexer.

Note: All acronyms are defined at the beginning of each Chapter

Chapter 1

Introduction

1.1 Motivation and State-of-the-Art

Information security is nowadays a high important research and development topic, since our personal, financial, and health data is transmitted over our communications networks. Moreover, highly sensitive commercial and national secrets are routinely being transmitted through the Internet [1]. To secure our digital data against an eavesdropper while it is transmitted, we can encrypt the data using a cryptographic key only known from the legitimate data users. Cryptographic keys are bit strings that should be random in such a way that no third party can determine the key [2]. The digital data that is encrypted with those keys can only be recovered using the original cryptographic key. An eavesdropper unknowing the cryptographic key will not be able to infer anything useful about the original data. In symmetric-key systems, the same key is shared by the transmitter and the receiver. In practice, the sender encrypts the sensible information using a random bit string, sends the encrypted data to the receiver, and the receiver decrypts the information using the same key. Notice that this process requires a preliminary stage where the encryption key is shared between the two parties [3]. However, this method presents a fundamental issue, namely, how the receiver will have access to the random cryptographic key generated by the transmitter. The process of sharing the key between the receiver and the transmitter is called key distribution [4]. This key transit, between the transmitter and the receiver, can be intercepted without the knowledge of the legitimate entities, enabling a third party to decode the information shared between them. In this context, Quantum Key Distribution (QKD) systems use the laws of quantum mechanics to enable the secure exchange of cryptographic keys. This is in contrast with conventional cryptography, whose security is based on the complexity of computational and mathematical algorithms. In QKD, the existence of an eavesdropper on a given communication channel is revealed since one cannot clone with maximum fidelity an unknown quantum state [5].

The development of QKD started in the 70s, while the first quantum cryptography protocol Bennett-Brassard 1984 (BB84) was proposed in 1984 [6]. Only in the late 80s, the practical implementation of this type of protocol was started [7]. Nevertheless, only during this century, its use in communication networks for sensitive information security started to be implemented, demanding a new era of communication technologies. Moreover, the practical evolution of quantum computers over the last few years has also stressed the need to increase the research of QKD systems [8]. This, mainly because the classical public key cryptography that is used in current networks will be deeply compromised by the possible forthcoming of a quantum computer running the Shor and/or Grover algorithms [9–11]. In this light, QKD systems have turned out to be a promising solution for secret data sharing,

offering unconditional security [12].

Information exchange is possible using optical fibers and free-space optical communication channels [13]. The BB84 protocol for QKD was implemented using the State of Polarization (SOP) of single photons [6]. Over the years more physical degrees-of-freedom of the electromagnetic field have been used for the same purpose, giving rise to more encoding methods in quantum cryptography, e.g. phase coding [3], frequency coding [14], polarization entanglement [15], and energy-time entanglement [3].

Polarization encoding presents advantages over the other mentioned encoding methods, namely for free-space optics applications [16]. When we consider an optical fiber as the quantum channel, maintaining a constant State of Polarization (SOP) of an optical signal has been the main issue for this encoding method [17]. The intrinsic residual birefringence presented in optical fibers, which is related to a loss of circular symmetry of the fiber-optic core [18], originates an undesired SOP drift, while extrinsic mechanisms cause that drift to be random over time, according to the environmental conditions in which the fiber is located, compromising the data transmission [19]. Some polarization drift compensation schemes have already been developed reducing the impact of this issue [20, 21]. Nevertheless, polarization encoding/decoding QKD systems are simpler to implement when compared with the phase or frequency encoding system counterparts.

Until now, the research activities addressing the optic fiber-based QKD systems have shown promising results regarding key metrics, e.g. the reach, key-rates, and practical implementations [22, 23]. This increased the efforts to develop efficient polarization encoding and decoding units to support the implementation of QKD protocols, e.g. the BB84 protocol [16]. The simplest way to generate the different SOPs, required to encode the quantum bits (qubits), is the use of multiple lasers, each one with a different SOP. However, this method suffers from side-channel information leakage [24]. Therefore, the development of efficient methods to generate stable polarization states is now of great importance, ensuring the quality of future polarization QKD systems. Several SOP generation schemes have been proposed, for example, using balanced Mach-Zehnder interferometers [25], or fiber-based Sagnac loops [24], among others. Even though the Mach-Zehnder scheme is simple to implement, it is highly unstable because of its sensitivity to environmental perturbations [24]. On the other hand, fiber-based Sagnac interferometers can generate highly stable SOPs, however, they present a complex experimental implementation [24].

This dissertation presents a new scheme for stable SOP generation using an Electronic Polarization Controller (EPC). The use of EPCs for SOP generation schemes presents a viable solution given their low insertion loss, low cost, small size, wavelength insensitivity, and plug and play versatility, overcoming several problems presented by other SOP generation schemes [16]. Also, a study of the mentioned SOP drift in optical links in differing environmental conditions is performed. This study is carried out to ensure the viability of polarization encoding methods. To quantify the SOP drift, a new parameter, designated as polarization linewidth [26], is calculated for different environments in this dissertation. The study of the SOP drift increases the understanding of the mechanisms that originate it, helping to find viable and efficient compensation solutions.

1.2 Dissertation Outline

This dissertation consists of five chapters. The thematics addressed in this work are divided as follows:

Chapter 1: This first chapter incorporates a state-of-the-art, in which a description of the development of QKD systems is made, mentioning previous works done on the subject,

referring to the motivation of this dissertation, the advantages of the methods used, and some objectives of this work.

Chapter 2: The second chapter addresses the theoretical formalisms, concepts, physical effects, and devices used in this work. First, the concept of light polarization is briefly introduced, with two of its most used mathematical description formalisms being presented and explained. Then, an explanation of how the polarization of light can be used to encode and decode information is made. After, the operation principle of QKD systems is briefly introduced. The SOP evolution in optical fibers is described, namely through the presentation of the mechanisms that cause the SOP drift and through the presentation of a theoretical evolution model that statistically describes the SOP drift in optical fibers.

Chapter 3: The third chapter initiates the experimental part of this dissertation, where some of the experimental techniques, such as the used apparatus and experimental setups, are specified and explained. The experimental conditions in which the measurements were made are also pointed out, and the experimental results for different environments are then presented. Lastly, a discussion of the results presented in this chapter is made.

Chapter 4: The fourth chapter focuses on the SOP generation based on EPCs, comprising both hardware and software implementations. This includes a theoretical description of the method used to generate different SOPs. Moreover, the mathematical description of an EPC and its experimental characterization is made. Also, the integration of the developed algorithm into a practical QKD system is presented.

Chapter 5: The fifth chapter summarizes the main results of this work, presents the main conclusion, and points out some future work.

1.3 Main Contributions

The most important contributions of this dissertation, compared to other studies in the field, are:

- Characterization of the polarization time drifts in two in-field experiments.
- Development, implementation, and validation of a new algorithm for SOP generation using an EPC.
- Integration of the proposed algorithm into a Discrete-Variable (DV) QKD system with polarization encoding.

1.4 Publications Related With This Work

S. T. Mantey, M. F. Ramos, N. A. Silva, A. N. Pinto, N. J. Muga, Algorithm for State-of-Polarization Generation in Polarization-Encoding Quantum Key Distribution, Accepted for presentation in the Telecoms Conference (ConfTELE), Leiria, 11–12 February 2021.

N. J. Muga, M. F. Ramos, S. T. Mantey, N. A. Silva, A. N. Pinto, FPGA-Assisted State-of-Polarization Generation for Polarization-Encoded Optical Communications, IET Optoelectronics, Vol. 14, No. 6, pp. 350–355, 2020.

N. J. Muga, M. F. Ramos, S. T. Mantey, N. A. Silva, A. N. Pinto, Deterministic State-of-Polarization Generation for Polarization-Encoded Optical Communications, Microwave and Optoelectronics Conference (IMOC) SBMO/IEEE MTT-S International, Aveiro, 2019.

Chapter 2

Theoretical Background

This chapter will briefly present the main theoretical concepts addressed in this dissertation. As the polarization of light is one of the main focus, this will be the first physical concept to be explained. Moreover, two polarization representation formalisms to describe the State of Polarization (SOP) will be presented. Further on, an explanation of how polarization is used to encode information to be applied in Quantum Key Distribution (QKD) systems will be introduced. Finally, a brief description of the evolution of the SOP in optical fibers will be presented.

2.1 Polarization Representation Formalisms

Light is an electromagnetic wave and polarization is one of the different observables that characterizes it, such as the intensity or the wavelength [27]. A fundamental difference between polarization and the intensity, or wavelength, of an electromagnetic wave is that the polarization is not a scalar quantity. The vectorial nature of light is what is called polarization [27]. Therefore, the polarization of light refers to the behavior of the electromagnetic field vector over time, observed at a fixed point in space [28].

An electromagnetic wave is said to be transverse when its electric field is perpendicular to the direction of wave propagation. The direction of the electric field defines the polarization of light, and the polarization in a given time instance in space is called the SOP. Considering Fresnel's wave theory, the electric field consists of two orthogonal components [29], the x and y components, which are the projection of the electric field vector on the x- and y-axis, respectively. The most general SOP is the elliptical polarization, where each component is defined by a given amplitude and phase [29]. Linear and circular polarization are specific cases of elliptical polarization. When the orientation of the electric field remains constant over time, linear polarization is observed, whereas, for an electric field orientation that varies, and if the amplitudes of the two components are equal, we observe a circular polarization. For QKD systems, linearly and circularly polarized light can be used to encode the information, given that these polarizations are mutually unbiased [30]. The QKD and polarization encoding systems will be explained in the following sections.

The two most used formalisms to describe the SOP are the Jones and the Stokes formalisms. The Jones formalism is obtained from the mathematical description of the phase and amplitude of the light being analysed, whereas the Stokes formalism is based on intensity measurements of the same light [31]. As the Jones formalism uses the phase and amplitude, this method can be used to study the combination of two non-coherent waves, for example in interferometers. The Stokes formalism, on the other hand, does not allow that study,

only the combination of coherent beams, for example, in a situation where we have various independent light sources, and where the beams are not superposed [27]. Another difference between these two methods is the ability to handle different degrees of polarization. While the Stokes formalism can describe light in its natural state, from a partially polarized state up to a full polarized state, the Jones formalism can only describe full polarized light [27]. When light is referred to as being in its natural state, it is meant that it is unpolarized so that the direction of the polarization fluctuates randomly and, on average, no particular direction is predominant. On the other hand, full polarized light is when only one direction of polarization is present, while partially polarized light consists in a intermediate state between full polarized and unpolarized light. In this section, both of the formalisms will be presented such as their mathematical description.

2.1.1 Jones Formalism

The Jones formalism describes the SOP by a two-dimensional complex vector that contains the phase and amplitude of light of both x and y components of the electric field, $E_x(z,t)$ and $E_y(z,t)$, respectively. Thus, the Jones vector can be written as follows [27]:

$$\mathbf{E} = \begin{pmatrix} E_x(z,t) \\ E_y(z,t) \end{pmatrix} = \begin{pmatrix} E_{0x}e^{i(wt-kz+\delta_x)} \\ E_{0y}e^{i(wt-kz+\delta_y)} \end{pmatrix}, \tag{2.1}$$

where t represents the time, z is the propagation distance, w is the optical frequency, k is the wave vector, δ_x and δ_y are the phases of the x and y components of the wave, respectively, and E_{0x} and E_{0y} represent the amplitudes of the x and y components, respectively. After suppressing the propagation term $wt-kz$ in equation (2.1), the Jones vector can be rewritten as [27]:

$$\mathbf{E} \equiv |\mathbf{E}\rangle = \begin{pmatrix} E_x \\ E_y \end{pmatrix} = \begin{pmatrix} E_{0x}e^{i\delta_x} \\ E_{0y}e^{i\delta_y} \end{pmatrix}. \tag{2.2}$$

E_x and E_y are complex quantities, the Jones vector acquires its imaginary component through the exponential term. To normalize the vector represented in (2.2) it is assumed that the intensity of the wave is given by $I = E_{0x}^2 + E_{0y}^2 = E_0^2$, where E_0^2 is usually considered equal to 1 when properly normalized [27].

Taking as an example the linear horizontal polarization, where there is no electric field along the y-axis, see Fig. 2.1, the respective Jones vector is written as:

$$|\mathbf{E}\rangle = \begin{pmatrix} E_{0x}e^{i\delta_x} \\ 0 \end{pmatrix}, \tag{2.3}$$

Normalizing the vector in (2.3), considering $E_{0x}^2 = 1$, and as $e^{i\delta_x}$ has a norm of 1, the Jones vector for horizontal polarization can be rewritten as shown in (2.4) by $|H\rangle$. Similarly, the Jones vectors for the vertical ($|V\rangle$), diagonal ($|+45\rangle$), anti-diagonal ($|-45\rangle$), right-hand circular ($|R\rangle$), and left-hand circular ($|L\rangle$) SOP can be determined as follows:

$$|H\rangle = \begin{pmatrix} 1 \\ 0 \end{pmatrix}, \tag{2.4}$$

$$|+45\rangle = \frac{1}{\sqrt{2}} \begin{pmatrix} 1 \\ 1 \end{pmatrix}, \tag{2.5}$$

$$|R\rangle = \frac{1}{\sqrt{2}} \begin{pmatrix} 1 \\ i \end{pmatrix}, \tag{2.6}$$

$$|V\rangle = \begin{pmatrix} 0 \\ 1 \end{pmatrix}, \tag{2.7}$$

$$|-45\rangle = \frac{1}{\sqrt{2}} \begin{pmatrix} 1 \\ -1 \end{pmatrix}, \tag{2.8}$$

$$|L\rangle = \frac{1}{\sqrt{2}} \begin{pmatrix} 1 \\ -i \end{pmatrix}. \tag{2.9}$$

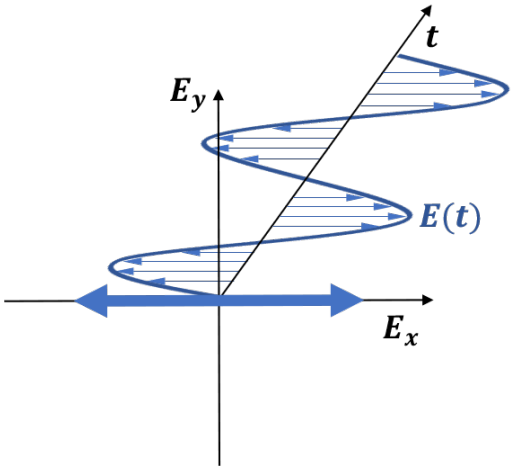

Figure 2.1: Schematic representation of the time evolution of an optical field linearly polarized along the x-axis.

The Jones matrices describe the polarization variation that an optic component induces and, therefore, they represent the transfer function of such an optical component, relating the input SOP with the output SOP. Given that the Jones matrices have dimension 2×2, and as the elements of the matrices are complex, there are eight variables to describe the eight existing types of polarization behavior [27]. To determine the Jones matrices it is assumed that the output components of the light beam that arises from the optical elements are linearly related to the incident beam. Therefore, one can write the following relation [27]:

$$|\mathbf{E}'\rangle = \begin{pmatrix} E'_x \\ E'_y \end{pmatrix} \equiv \boldsymbol{J}\,|\mathbf{E}\rangle = \begin{pmatrix} j_{xx} & j_{xy} \\ j_{yx} & j_{yy} \end{pmatrix} \begin{pmatrix} E_x \\ E_y \end{pmatrix}, \tag{2.10}$$

where $|\mathbf{E}'\rangle$ represents the output electric field, E'_x and E'_y are the components of the electric field at the output of the optical element, E_x and E_y are the components at its entrance, and $\boldsymbol{J}$ is the Jones matrix representing the optical element, whose complex entries are given by j_{xx}, j_{xy}, j_{yx}, and j_{yy}.

Hereafter, we will use *kets* ($|\cdot\rangle$) to represent the Jones vectors.

2.1.2 Stokes Formalism

One alternative polarization description method to the Jones formalism is the Stokes formalism [32]. This formalism describes the SOP using four quantities called the Stokes parameters. The Stokes parameters are directly obtained from intensity measurements of the light beam, being this way real quantities, on the contrary of what happens in the Jones formalism. Mathematically these parameters can be represented as follows [27]:

$$S_0 = E_{0x}^2 + E_{0y}^2, \tag{2.11}$$
$$S_1 = E_{0x}^2 - E_{0y}^2, \tag{2.12}$$
$$S_2 = 2E_{0x}^2 E_{0y}^2 \cos(\delta), \tag{2.13}$$
$$S_3 = 2E_{0x}^2 E_{0y}^2 \sin(\delta), \tag{2.14}$$

where E_{0x} and E_{0y} are the same as defined in (2.2), in the previous section, δ is the phase difference of the wave such that $\delta = \delta_y - \delta_x$. From the above-written equations, it is possible to verify that S_0 is the total intensity of the light beam, S_1 quantifies the light with linear horizontal versus with linear vertical polarization, which can be obtained by calculating the difference between intensities of the signal measured after it passes through a linear horizontal and a linear vertical polarizer, S_2 describes the quantity of linear $+45°$ or $-45°$ polarized light, obtained from the difference between intensities of the signal measured after it passes through a linear $+45°$ and $-45°$ polarizer, and, lastly, S_3 describes the quantity of light with right- or left-hand circular polarization, in this case, obtained from the difference of intensities of the signal measured after it passes through of a right- and left-hand circular polarizer [33, 34]. Considering the above description of the Stokes parameters, the Stokes vector is written as a 4-dimensional vector:

$$\mathbf{S} = \begin{pmatrix} E_{0x}^2 + E_{0y}^2 \\ E_{0x}^2 - E_{0y}^2 \\ 2E_{0x}^2 E_{0y}^2 \cos(\delta) \\ 2E_{0x}^2 E_{0y}^2 \sin(\delta) \end{pmatrix}. \tag{2.15}$$

Considering again the linear horizontal polarization as an example, where $E_{0y}^2 = 0$, the Stokes vector (2.15) is written as:

$$\mathbf{S}_H = I \begin{pmatrix} 1 \\ 1 \\ 0 \\ 0 \end{pmatrix}, \tag{2.16}$$

where I is the total intensity of the beam and $I = E_{0x}^2$. From (2.15), by normalizing the Stokes vector to I it is possible to define a 3-dimensional normalized Stokes vector, $\mathbf{s}$, whose entries are given by $s_i = S_i/S_0$, with $i = 1$, 2, and 3 [34].

A key advantage of this formalism is the representativeness of the SOP on the Poincaré sphere, as shown in Fig. 2.2. To represent a Stokes vector on the Poincaré sphere the three Stokes parameters, s_1, s_2, and s_3, have to be seen as the coordinates of a point over the surface of the sphere. Using this representation, every existing SOP can be represented by a single point on the surface of this sphere. The equator of the Poincaré sphere holds for all the linear SOPs (that is, for $s_3 = 0$), while the poles hold for the circular polarization (right-hand circular on the north pole and left-hand circular on the south pole), the points lying between the equator and the poles represent elliptic SOPs [29].

The Stokes formalism can also represent the interaction of optical components with light through matrices. It is assumed that the Stokes vector of the incident beam, $\mathbf{S}$, characterized by the Stokes parameters S_i, with $i = 0, 1, 2$ and 3, exhibits a linear dependency with the output Stokes vector, $\mathbf{S}'$, after interacting with an optical component. This linear dependency can be written as [27]:

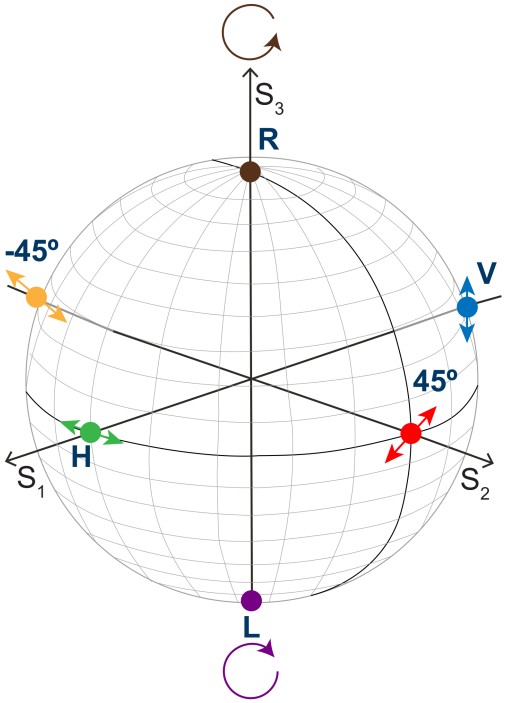

Figure 2.2: Poincaré sphere with the 6 SOPs: $|H\rangle$ - horizontal; $|V\rangle$ - vertical; $|+45\rangle$ - diagonal; $|-45\rangle$ - anti-diagonal; $|R\rangle$ - right-hand circular; $|L\rangle$ - left-hand circular.

$$S_0' = m_{00}S_0 + m_{01}S_1 + m_{02}S_2 + m_{03}S_3, \tag{2.17}$$
$$S_1' = m_{10}S_0 + m_{11}S_1 + m_{12}S_2 + m_{13}S_3, \tag{2.18}$$
$$S_2' = m_{20}S_0 + m_{21}S_1 + m_{22}S_2 + m_{23}S_3, \tag{2.19}$$
$$S_0' = m_{30}S_0 + m_{31}S_1 + m_{32}S_2 + m_{33}S_3, \tag{2.20}$$

where m_{ji}, with $i, j = 0, ..., 3$, are the Muller coefficients. By writing the system of equations from (2.17) to (2.20) in the matrix form, the following is obtained:

$$\begin{pmatrix} S_0' \\ S_1' \\ S_2' \\ S_3' \end{pmatrix} = \begin{pmatrix} m_{00} & m_{01} & m_{02} & m_{03} \\ m_{10} & m_{11} & m_{12} & m_{13} \\ m_{20} & m_{21} & m_{22} & m_{23} \\ m_{30} & m_{31} & m_{32} & m_{33} \end{pmatrix} \begin{pmatrix} S_0 \\ S_1 \\ S_2 \\ S_3 \end{pmatrix} \equiv \mathbf{S}' = \boldsymbol{M} \cdot \mathbf{S}, \tag{2.21}$$

where $\boldsymbol{M}$ is the Mueller matrix, with dimension 4×4. On the Poincaré sphere, a SOP change is translated into a rotation of the point on the sphere, therefore, the Mueller matrices are also known as rotation matrices with dimension 3×3. Notice that for a system that only presents unitary transformations, i.e. no gain and no polarization-dependent losses, the matrix $\boldsymbol{M}$ can be written as a 3×3 dimension matrix, instead of 4×4 [35].

The transfer matrices of the two presented formalisms, Jones and Stokes, can be related using Pauli's spin matrices. For instance, the elements of the Mueller matrix can be determined from the Jones matrix using the following expression [34, 36]:

$$m_{ij} = \frac{1}{2}\mathrm{Tr}(\boldsymbol{J}\sigma_j\boldsymbol{J}^T\sigma_i), \tag{2.22}$$

where $\mathrm{Tr}(x)$ denotes the trace of the matrix x, the superscript T denotes the conjugate, and σ_i, with $i = 1...3$, are the Pauli matrices, defined as [27]:

$$\sigma_0 = \begin{pmatrix} 1 & 0 \\ 0 & 1 \end{pmatrix},\ \sigma_1 = \begin{pmatrix} 0 & 1 \\ 1 & 0 \end{pmatrix},\ \sigma_2 = \begin{pmatrix} 0 & -i \\ i & 0 \end{pmatrix},\ \sigma_3 = \begin{pmatrix} 1 & 0 \\ 0 & -1 \end{pmatrix}. \tag{2.23}$$

In both formalisms, Jones and Stokes, an optical system comprised by the concatenation of various optical components can be mathematically represented by the product of the n matrices that characterize the different optical components of the system. In the Stokes formalism, such a system can be described by the following expression [36]:

$$\boldsymbol{M} = \boldsymbol{M}_n \boldsymbol{M}_{n-1} \dots \boldsymbol{M}_2 \boldsymbol{M}_1. \tag{2.24}$$

2.2 Polarization in QKD systems

This section addresses the use of the SOP of an optical signal to encode information in quantum systems. For particular polarizations, we present the polarization encoding and decoding subsystems, how they can be applied in a QKD system, and the Quantum Bit Error Rate ($QBER$) as a metric to quantify the quality of the qubit transmission.

2.2.1 Polarization Encoding and Decoding

In a quantum information transmission system, there is an emitter (usually called Alice), a receiver (usually called Bob), and a quantum channel, where the information is transported by qubits. To describe these systems mathematically, the state of the qubit is represented as $|\Phi\rangle$, such that [37]:

$$|\Phi\rangle = \alpha\,|0\rangle + \beta\,|1\rangle\,. \tag{2.25}$$

The base $|0\rangle, |1\rangle$ represent two eigenstates in which the qubit can be measured. The probability of measuring each one of the states ($|0\rangle$ or $|1\rangle$) is equal if $|\alpha| = |\beta| = \frac{1}{\sqrt{2}}$.

When information is encoded in the SOP the bases used for encoding are mutually non-orthogonal, however, the two eigenstates that can be measured in each base are orthogonal. The polarization is a Hilbert space with dimension 2. In that space, it is possible to define three mutually non-orthogonal bases. The rectilinear base (+), that is defined by the horizontal polarization, as represented in (2.4), and by the vertical polarization, as represented in (2.7). The diagonal base (×), non-orthogonal to the rectilinear base, defined by the diagonal polarization, represented in (2.5), and by the anti-diagonal polarization, as represented in (2.8). The circular base (○), non-orthogonal to the other two bases mentioned above, that is defined by the left-hand circular polarization, as represented in (2.9), and by the right-hand circular polarization, as represented in (2.6) [3].

After the previous agreement regarding the bases to be used in the selected quantum protocol, Alice can now send qubits to Bob through the quantum channel, typically an optical fiber. The quantum protocols, e.g. the QKD, take advantage of the uncertainty principle of Heisenberg and the no-cloning theorem [3]. The uncertainty principle and the no-cloning theorem make a QKD system unconditionally secure, preventing a third entity, usually called Eve, to read the transmitted information without being detected. The no-cloning theorem postulates that it is impossible to create an identical replica of a given state, being this way directly related to the uncertainty principle. This principle states that it is impossible to know some given pairs of physical properties, X and Y, with arbitrary precision, being the respective uncertainties, ΔX and ΔY, related as follows [38]:

$$\Delta X^2 \Delta Y^2 \geq \frac{1}{4} |\langle [\, X, Y \,] \rangle|^2\,, \tag{2.26}$$

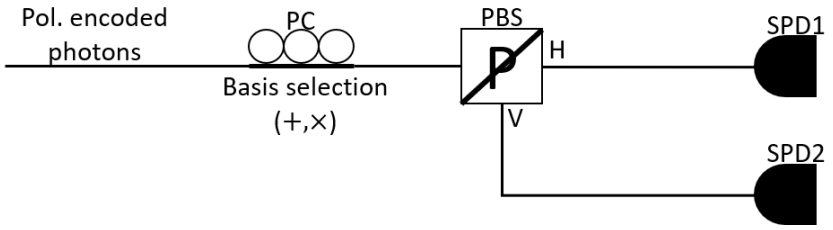

Figure 2.3: Schematic representation of a possible setup for a polarization decoding system. Polarization encoded photons are aligned by a PC with one base (rectilinear or diagonal). After, a PBS separates the differently polarized photons and directs them to the SPDs.

where $[X, Y] \equiv XY - YX$ is the commutator. Because of the uncertainty principle, it is not possible to know all characteristics of a given state, and as a result, the cloning of that state is impossible.

The decoding process in polarization-based QKD systems requires a method to determine the polarization of the incoming polarized photons. That can be done using a polarization decoding system, see Fig. 2.3, comprised by a Polarization Controller (PC), that aligns the receiver with the base in which the measurement will be made, a Polarization Beam Splitter (PBS), and two Single-Photon Detector (SPD)s, making it possible to distinguish between horizontal, vertical, diagonal and anti-diagonal polarization. After the PC, the PBS splits the beam into two polarized beams and directs them to the SPDs. Whether the SPD1 or the SPD2 clicks determines how the detected photon was polarized and allows to distinguish if a 0 or a 1 was sent.

2.2.2 Brief Description of a QKD System

In 1984, Bennett and Brassard proposed the first QKD protocol, presenting a new idea for an innovating key distribution system for cryptography purposes. That pioneering QKD protocol is known as the BB84 [6]. The proposed protocol was based on the idea of encoding the information in the SOP of single photons. Any eavesdropper would not be able to access the information without remaining undetected by Alice and Bob given the no-cloning theorem and the uncertainty principle. Fig. 2.4 illustrates the BB84 protocol.

The BB84 works as follows: Alice chooses a sequence of random bits and a random sequence of polarization basis, rectilinear (+) or diagonal (×), to encode each bit. She encodes the bits with the respective base using polarized photons and sends them to Bob over a quantum channel. Each base contains two polarization states, the rectilinear base contains the $|H\rangle$ and the $|V\rangle$ polarization state, while the diagonal base contains the $|+45\rangle$ and $|-45\rangle$ polarization state. Usually, $|H\rangle$ and $|+45\rangle$ represent a binary zero, and $|V\rangle$ and $|-45\rangle$ represent a binary one.

Bob chooses one base randomly, and independently from Alice, to measure each received photon. He interprets the measurements as zero or one and records the information and the respective base he used to measure each photon. After sending and measuring the qubits, Alice and Bob use a classical channel to share the bases used in the coding/decoding process. Therefore, if Bob measures a given photon with the wrong base, for example, a rectilinear photon with a diagonal base, the information of that photon is discarded during the bases agreement phase of the protocol. Therefore, as Bob's choice of basis is random, only half of the photons Bob receives represent meaningful information, corresponding to the measurements where Bob did the right base guess [6].

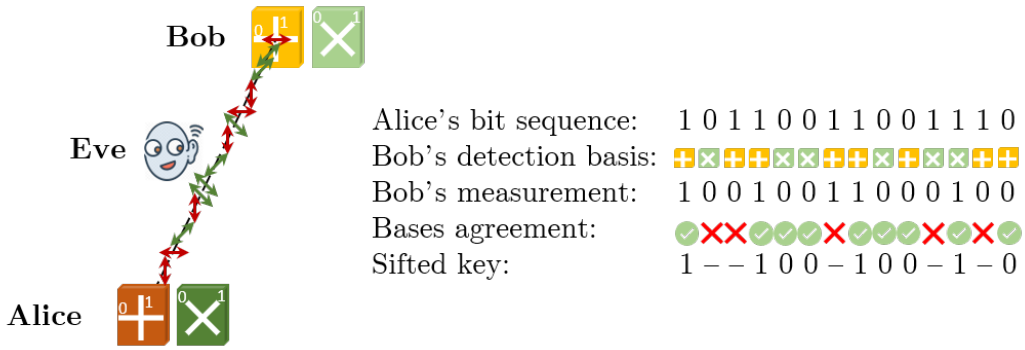

Figure 2.4: Schematic representation of the principle of the BB84 protocol. Alice chooses a random bit string and a random sequence of bases that is composed out of two possible polarization bases (rectilinear and diagonal). Each base has two polarization states, one corresponding to a binary one and the other to a binary zero. Alice encodes the bits and sends the polarized photons to Bob, who receives the photons and measures their polarization using, also, a randomly chosen basis for each photon. The basis that Bob used to obtain his bit sequence is then compared with the basis Alice used. The bits for which Bob chose the right basis compose the secret key. Eve represents the eavesdropper.

Over a public (classical) channel, that is considered to be susceptible to eavesdropping but not to alterations of the sent message, Alice and Bob determine which photons were effectively received. This verification is necessary given that some photons might get lost over the transmission or, as the detectors are not perfect, some photons might not be detected. After this step, Alice and Bob, remain with a secret key only known to them. Some of these bits can be transmitted using a classical channel, to compare them and verify if they agree. These control bits can be used to measure the quality of the transmission, by calculating, for example, the *QBER*, which will be explained in the next subsection.

2.2.3 Quantum Bit Error Rate

The *QBER* is a measure of the quality of the information transfer in a quantum communication system. This parameter is obtained by the ratio of wrong bits received, N_{wrong}, to the total received bits ($N_{\text{wrong}} + N_{\text{right}}$), as written, in terms of ratios, in the following equation [3]:

$$\text{QBER} = \frac{N_{\text{wrong}}}{N_{\text{wrong}} + N_{\text{right}}} = \frac{R_{\text{error}}}{R_{\text{error}} + R_{\text{sift}}}, \tag{2.27}$$

where R_{error} is the rate of error and R_{sift} corresponds to the rate of the sifted key, which relates to the raw key rate as $R_{\text{sift}} = 1/2 R_{\text{raw}}$, given that, statistically, Alice and Bob only make compatible base choices in half of the raw key [3]. The raw key rate and the sifted key rate can be written as:

$$R_{\text{sift}} = \frac{1}{2} R_{\text{raw}} = \frac{1}{2} f_{\text{rep}} \mu t_{\text{link}} \eta, \tag{2.28}$$

where f_{rep} is the pulse rate, μ is the mean number of photons per pulse, t_{link} is the probability of a photon arriving at the detector, that is, the transmission efficiency, and η is the probability of the photon being detected by the SPD [3].

There are three main identifiable contributions to the total error rate [3]:

- R_{opt} - This rate accounts for the probability of a photon going to the wrong detector, p_{opt}. R_{opt} can be calculated by the product of R_{sift} by the mentioned probability, such that:

$$R_{\text{opt}} = R_{\text{sift}} p_{\text{opt}}. \tag{2.29}$$

- R_{det} - This rate arises from dark counts of the detector, which corresponds to counts that were registered without any incident light. Only dark counts that occur in the short period in which a photon is expected to be detected, are accounted for this rate. R_{det} can be written such that:

$$R_{\text{det}} = \frac{1}{4} f_{\text{rep}} p_{\text{dark}} n, \tag{2.30}$$

  where p_{dark} is the probability of a dark count occurring, in one detector and one short period and n is the number of detectors. The $\frac{1}{4}$ has to do with the 50% probability of the dark count occurring in the right detector, plus, the 50% probability of the dark count occurring when Alice and Bob chose incompatible bases.

- R_{acc} - The last contribution to the total error rate arises due to imperfect photon sources. However, these error counts only occur in systems that handle entangled photons, which is not the case in this work, therefore, this rate will not be considered.

Finally, the total *QBER* can be expressed as follows:

$$\begin{aligned} \text{QBER} =& \frac{R_{\text{opt}} + R_{\text{det}}}{R_{\text{sift}}} && (2.31)\\ =& p_{\text{opt}} + \frac{p_{\text{dark}} n}{2\mu t_{\text{link}} \eta} && (2.32)\\ =& \text{QBER}_{\text{opt}} + \text{QBER}_{\text{det}}. && (2.33) \end{aligned}$$

The first term of (2.33), QBER_{opt}, is not affected by the transmission efficiency of the fiber link. This parameter can be used as a measure of the optical quality of the used setup and is usually around 1%, however, this value can be difficult to maintain given the polarization fluctuations and depolarization that can occur along the optical link. On the other hand, the second term, QBER_{det}, depends on the transmission efficiency given that the dark count rate increases with distance.

2.3 Evolution of the SOP in Optical Fibers

Currently, QKD systems are mainly supported by optical fibers that act as the quantum channel. Optical fibers are made of silica and are composed by a core, in which the light is guided, embedded in an outer cladding with a slightly lower refractive index. Such refractive index difference permits the total internal reflection of light inside the core, enabling the transmission of light through the fiber for long distances with a typical attenuation value around 0.2 dB/km in the 1550 nm spectral window [39]. In general, the optical signal propagation in this waveguide is affected by several effects, such as attenuation, dispersion, polarization effects, and nonlinear effects. However, the dispersion and the nonlinear effects are negligible in quantum links. On the other hand, attenuation plays a key role in fiber-optic QKD systems as it limits the reach of QKD systems. Regarding the polarization effects, they represent a compromising factor for polarization-encoded QKD as they may lead to misalignment between the polarization referential of Alice and Bob. There are many

effects that change the polarization of a signal when propagating in an optical fiber. The most relevant effect is the birefringence. As some of the birefringence mechanisms are due to non-predictable environmental perturbations, stochastic evolution models must be used to assess the effect of such mechanisms on the polarization [26].

2.3.1 Birefringence Mechanisms

A perfectly isotropic fiber would not exhibit birefringent effects, therefore, the polarization of the output signal would be the same as the polarization of the input signal [40]. However, the fibers installed in the field are not perfect, exhibiting non-negligible values of birefringence.

There are two types of mechanisms causing birefringence in fibers: intrinsic and extrinsic mechanisms. The main difference between these two types of birefringent mechanisms lays in their dependence on time: intrinsic mechanisms are, usually, constant over time, while extrinsic mechanisms vary over time. The intrinsic mechanisms can occur due to imperfections of the fiber possibly caused by the fabrication process, for example, core ovality, internal stress, micro-bubbles, or impurity concentrations, as schematically represented by Fig. 2.5 (a) i), ii) and iii), respectively [31]. The extrinsic mechanisms, on the other hand, induce imperfections to the fiber because of environmental perturbations. For example, wind, temperature variation, mechanic stress, among others, cause tensions that can curve, squeeze, or twist the fiber, as schematically shown by Fig. 2.5 (b) i), ii) and iii), respectively [34]. These last-mentioned mechanisms fluctuate over time.

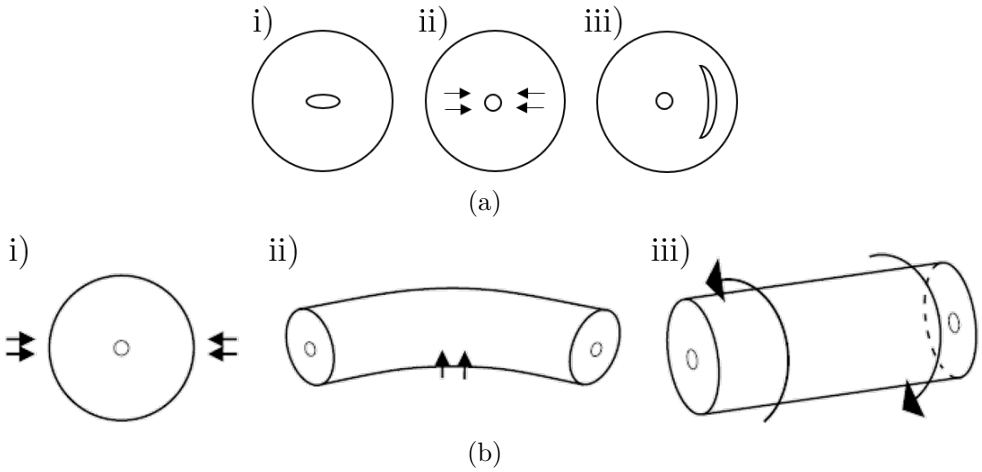

Figure 2.5: (a) Intrinsic birefringence mechanisms in optical fibers; i) Core ovality; ii) Internal stress; iii) Micro-bubbles or impurity concentrations; (b) Extrinsic birefringence mechanisms in optical fibers; i) Squeezing; ii) Bending; iii) Twisting. Adapted from [31] and [34].

The above-mentioned fiber imperfections cause a loss of symmetry of the fiber core, such that the two orthogonal directions x and y will have different effective refractive indexes. This refractive index anisotropy leads to polarization changes [40].

Extrinsic mechanisms are therefore the most problematic birefringence mechanisms, particularly for polarization-encoding QKD systems, given that they depend on many variables that alter the input SOP in a non-predictable way. Given the huge amount of variables that induce birefringence over time and space, the SOP variation can be considered random and needs to be described by stochastic evolution models [26].

2.3.2 Stochastic Evolution Modeling

To model the evolution of the SOP we are going to use the Stokes formalisms, taking advantage of the easier visualization of the SOP change on the Poincaré sphere. This evolution model emulates a random walk on the Poincaré sphere, accounting for random polarization drifts, based on a method described by [26]. There are other models that emulate the random polarization drift, however, most of them introduce deterministic changes in the SOP [41–44], or use a constant randomly chosen SOP for polarization demultiplexing [45–48], and do not study the behavior of an unbiased SOP. Moreover, there are statistical models to describe the differential group delay and polarization-mode dispersion, however, using intensity modulation or single-polarization phase shift keying formats, which are not affected by the SOP drift [49]. Literature also presents some works where direct measurements of fast SOP changes were made, however, these SOP changes were induced in a dispersion compensating module in the laboratory and do not consider the random drift of the SOP in an entire optical link [50]. The model presented by [26] is the first one that emulates the random drift of the SOP, it assumes that the polarization drift can be described by a succession of random Jones or Mueller matrices, depending on the formalism used, where each one of the transfer matrices is parametrized by three random parameters that follow a normal distribution.

As described in section 2.1.2, a unitary propagation of the optical field can be described by a 3×3 Muller matrix $\boldsymbol{M}$. The evolution of the SOP vector is considered to be as follows:

$$\mathbf{r}_k = \boldsymbol{M}_k \mathbf{u}_k, \tag{2.34}$$

where $\mathbf{r}_k$ is the output SOP after the actuation of the evolution Mueller matrix $\boldsymbol{M}_k$ on the input SOP, $\mathbf{u}_k$, and k denotes the iteration number. The Mueller matrix in (2.34) can be written as $\boldsymbol{M}_k = M(\boldsymbol{\alpha}_k)$, where $M(\cdot)$ is expressed as an exponential function, with $\boldsymbol{\alpha} = (\alpha_1, \alpha_2, \alpha_3)$ being a vector of parameters that model the random fluctuations of the SOP, such that [26]:

$$\begin{aligned} M(\boldsymbol{\alpha}) &= \exp(2\mathcal{K}(\boldsymbol{\alpha})) && (2.35)\\ &= \exp(2\theta\mathcal{K}(\mathbf{a})) && (2.36)\\ &= \boldsymbol{I}_3 + \sin(2\theta)\mathcal{K}(\mathbf{a}) + \left[1 - \cos(2\theta)\right]\mathcal{K}(\mathbf{a})^2, && (2.37) \end{aligned}$$

where $\boldsymbol{I}_3$ is the identity matrix with dimension 3×3, θ is the length of $\boldsymbol{\alpha}$, so $\theta = \|\boldsymbol{\alpha}\|$, being also the angle of rotation of the Poincaré sphere that represents the SOP transformation, $\mathbf{a}$ is a unit vector, such that $\mathbf{a} = (a_1, a_2, a_3)$ represents the direction of $\boldsymbol{\alpha}$. These three parameters can be related such that $\boldsymbol{\alpha} = \theta\mathbf{a}$. In (2.35)–(2.37) $\mathcal{K}(\mathbf{a})$ denotes [26]:

$$\mathcal{K}(\mathbf{a}) = \begin{pmatrix} 0 & -a_3 & a_2 \\ a_3 & 0 & -a_1 \\ -a_2 & a_1 & 0 \end{pmatrix}. \tag{2.38}$$

The time evolution of $\boldsymbol{M}_k$ is described as:

$$\boldsymbol{M_k} = M(\dot{\boldsymbol{\alpha}}_k)\boldsymbol{M}_{k-1}, \tag{2.39}$$

where $M(\dot{\boldsymbol{\alpha}}_k)$ is a random innovation matrix and $\dot{\boldsymbol{\alpha}}_k$ is a random vector with a zero mean normal distribution, such that $\dot{\boldsymbol{\alpha}}_k \sim \mathcal{N}(0, \sigma_p^2\mathbf{I}_3)$, with σ_p^2 being the variance of the distribution. The variance, σ_p^2, can be defined as follows [26]:

$$\sigma_p^2 = 2\pi\Delta pT, \tag{2.40}$$

where Δp is the polarization linewidth, which quantifies the speed of the SOP drift, and T is the sampling period.

For the simulations, the vector $\boldsymbol{\alpha}$ was generated using the *randn*$(3, k)$ function of *Matlab*, which creates a $3\times k$ array of normally distributed random numbers, to simulate the randomness of the SOP drift. In a first analysis, we have used a variance of $\sigma_p^2 = 6\times10^{-4}$ ($\Delta p = 4\times10^{-5}$), a period of 2.2 hours, and the initial Stokes vector was assumed to be $(0, 0, 1)^T$. Figs. 2.6 and 2.7 show the evolution of the modeled SOP for (a) 300 iterations, (b) 1500 iterations and (c) 3000 iterations. While Fig. 2.6 represents the Stokes parameters time drift on the Poincaré sphere, Fig. 2.7 shows the same of each parameter s_1, s_2 and s_3. The color gradient in Fig. 2.6 represents the time evolution, such that the initial SOPs are represented as red dots and at the end as yellow dots. From Figs. 2.6 and 2.7, it is possible to observe the

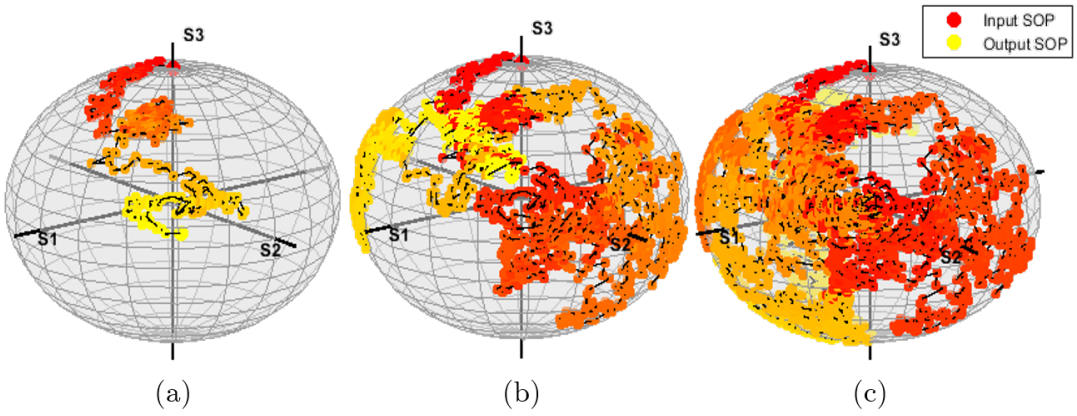

Figure 2.6: Stochastic evolution of the SOP drift, represented on the Poincaré sphere, obtained by (2.34), with $\sigma_p^2 = 6 \times 10^{-4}$, a period of 2.2 hours, and using an input Stokes vector of $(0, 0, 1)^T$. The evolution model was made for: (a) 300 iterations; (b) 1500 iterations; (c) and 3000 iterations. The color variation from red to yellow represents the time evolution, where red is the beginning SOP and yellow the end SOP.

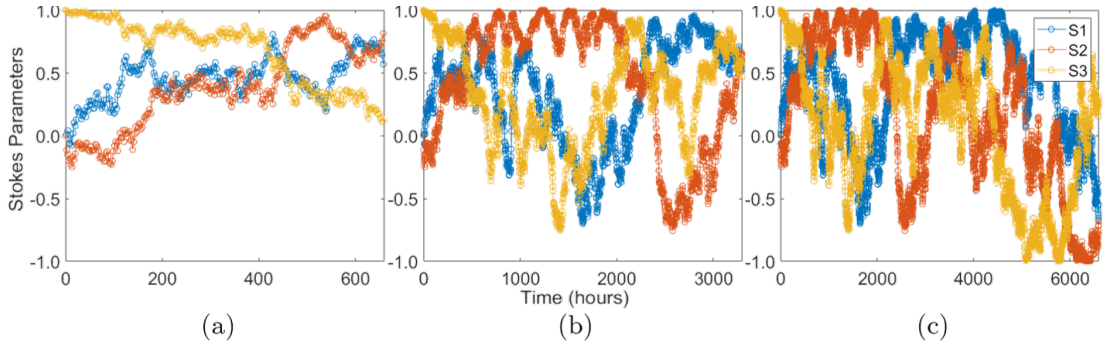

Figure 2.7: 2D time evolution of the Stokes parameters presented in Fig. 2.6, for a variance of $\sigma_p^2 = 6 \times 10^{-4}$, a period of 2.2 hours, using an input Stokes vector of $(0, 0, 1)^T$ and a number of iterations of: (a) 300, (b) 1500, and (c) 3000.

randomness of the polarization drift, where each SOP is independent of the previous SOP and has an equal probability for every direction. The speed of the drift can be characterized by the variance that is set by the polarization linewidth parameter, Δp, as referred to in (2.40).

In order to assess the real impact of the parameter Δp on the speed of the SOP drift, we have performed a set of simulations considering different values for this parameter. Figs. 2.8 and 2.9 show the obtained SOPs represented on the Poincaré sphere and its 2D representation, respectively, for different variance values: (a) $\sigma_p^2 = 6\times10^{-5}$ ($\Delta p = 4\times10^{-6}$), (b) $\sigma_p^2 = 6\times10^{-4}$ ($\Delta p = 4 \times 10^{-5}$), and (c) $\sigma_p^2 = 6 \times 10^{-3}$ ($\Delta p = 4 \times 10^{-4}$). The three plots have the same number of iterations: 1500. A period of 2.2 hours was used and the initial Stokes vector was $(0, 0, 1)^T$. Results show that higher values of the variance induce faster time drifts in the SOP of the optical signal.

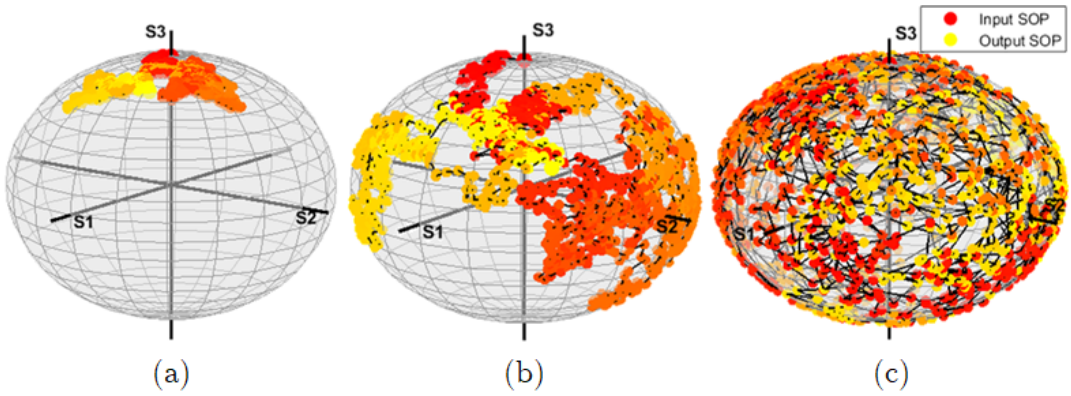

Figure 2.8: Stochastic evolution of the SOP drift, represented on the Poincaré sphere, obtained by (2.34), with 1500 iterations, a period of 2.2 hours, and using an input Stokes vector of $(0, 0, 1)^T$. The evolution models were made for a variance of: (a) $\sigma_p^2 = 6 \times 10^{-5}$, (b) $\sigma_p^2 = 6 \times 10^{-4}$, and (c) $\sigma_p^2 = 6 \times 10^{-3}$. The color variation from red to yellow represents the time evolution, where red is the beginning and yellow the end.

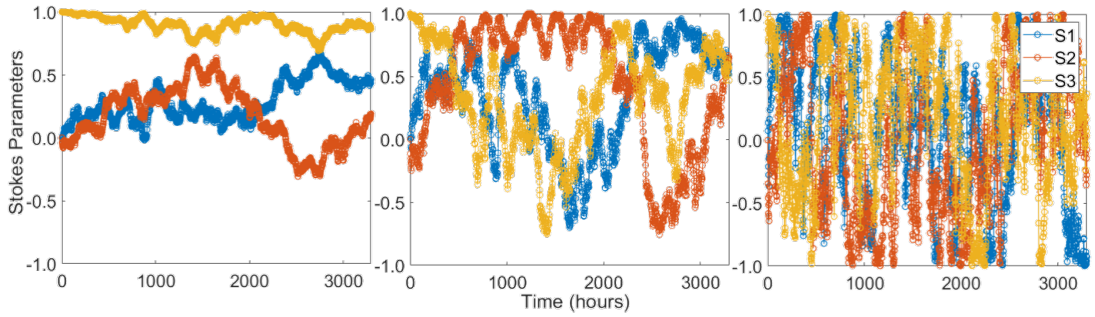

Figure 2.9: 2D time evolution of the Stokes parameters presented in Fig. 2.8, with 1500 iterations, a period of 2.2 hours, using an input Stokes vector of $(0, 0, 1)^T$ and a variance of: (a) $\sigma_p^2 = 6 \times 10^{-5}$, (b) $\sigma_p^2 = 6 \times 10^{-4}$, and (c) $\sigma_p^2 = 6 \times 10^{-3}$.

2.3.3 Polarization Linewidth and Autocorrelation Function

As referred in the previous Section 2.3.2, the polarization linewidth parameter, Δp, determines the speed of the SOP drift and it is dependent on the details of the system. Thus, to characterize the random SOP drift of a given system during the information transmission process using optical fibers, the parameter Δp can be used. Hence, the Δp can be determined by calculating the Autocorrelation Function (ACF) between the various SOPs, using

the definition presented in [26]. The ACF quantifies the correlation that exists between a pair of samples taken at different time instances of a random process and it is obtained by calculating the expected value of the product of two Stokes vectors corresponding to two samples. Using the Stokes formalism, the ACF of the random drift of SOPs can be determined as follows [26]:

$$\begin{aligned} \mathrm{ACF}(l) &= \mathbb{E}[\mathbf{r}_k^T \mathbf{r}_{k+l}] && (2.41)\\ &= \mathbb{E}[(\boldsymbol{M}_k \mathbf{u})^T \boldsymbol{M}_{k+l} \mathbf{u}] && (2.42)\\ &= \|\mathbf{u}\|^2 \left(\frac{2(1-4\sigma_p^2)\exp(-2\sigma_p^2)+1}{3} \right)^{|l|}, && (2.43) \end{aligned}$$

where $\mathbb{E}[\cdot]$ denotes the expected value, $\mathbf{r} = \boldsymbol{M}_k \mathbf{u}$, $\mathbf{u}$ being the input SOP, k is the iteration, l is the normalized time separation between samples such that lT is the absolute time separation, and $\boldsymbol{M}_k$ is the transfer function matrix. In (2.43), σ_p^2 is the variance of the zero-mean Gaussian adjustment distribution for the SOPs time evolution. When $\sigma_p \ll 1$, the following approximations are possible [26]:

$$\exp(-2\sigma_p^2) \approx 1 - 2\sigma_p^2, \tag{2.44}$$

$$\sigma_p^4 \approx 0, \tag{2.45}$$

$$(1 - 8\pi|l|\, T\Delta p/|l|)^{|l|} \approx \exp(-8\pi|l|\, T\Delta p). \tag{2.46}$$

By using the three previous approximations into (2.43), the ACF can be written as [26]:

$$\mathrm{ACF}(l) \approx \|\mathbf{u}\|^2 \exp(-8\pi|l|\, T\Delta p). \tag{2.47}$$

Equation (2.47) was used in order to adjust an exponential curve to the numerical data. After obtaining the equation of the adjusted curve it is possible to extract the respective Δp parameter. In conclusion, this model can be used to characterize the SOP stability of certain fiber-optic links, and, therefore, it is useful to support polarization encoded QKD systems. In the next chapter, we are going to use this technique to calculate the Δp parameter of two fiber links installed in two different cities.

Fig. 2.10 shows the representation of several ACFs, obtained from a set of five runs. The simulated ACF curves were determined from simulated data that was obtained using the method described in Section 2.3.2, using the same parameters: a variance of $\sigma_p^2 = 6 \times 10^{-4}$, a $T = 2.2$ hours, and 3001 iterations. However, the ACF was determined only for 1/4 of the generated SOPs, corresponding to $|l| = 0, ..., 750$. Higher fractions would cause imprecisions. It is possible to see that the simulated ACF curves, oscillate around the theoretical curve, that was obtained using (2.47).

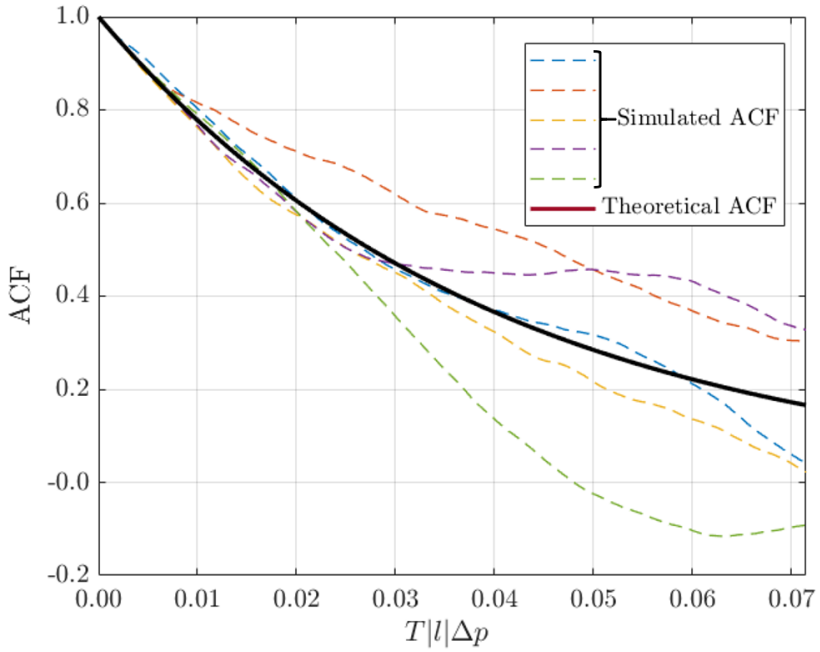

Figure 2.10: Theoretical ACF, (2.47), with $T = 2.2$ hours, a variance of $\sigma_p^2 = 6 \times 10^{-4}$ and 3000 iterations. The simulated ACFs were obtained from a set of five runs using the same parameters as the theoretical ACF.

Chapter 3

Experimental Assessment of Polarization Drift in Quantum Links

In this chapter, the practical implementation of the polarization drift measurements for the assessment of quantum links will be discussed. Initially, a brief description of the experimental techniques and apparatus will be presented. Regarding the experimental SOP drift results, we will start by presenting the measurements obtained in the laboratory and after we will present the field measurements in two different locations.

3.1 Electro-Optic and Polarization Techniques

In order to accomplish the experimental part of this dissertation, several techniques and apparatus were used. Hence, before presenting the experimental results, the most relevant techniques and apparatus used for the polarization drift measurements, such as the polarimeter and the Optical Time-Domain Reflectometer (OTDR), will be briefly described.

3.1.1 Polarimeter

A polarimeter is an opto-electronic device that allows measuring the Stokes parameters of an optical field. This device comprises three fundamental elements, a rotating Quarter Waveplate (QWP), a Linear Polarizer (LP), and a p-i-n Photodiode (PIN), arranged in proper order, as shown in Fig. 3.1. In the following section, the working principle of these elements is described.

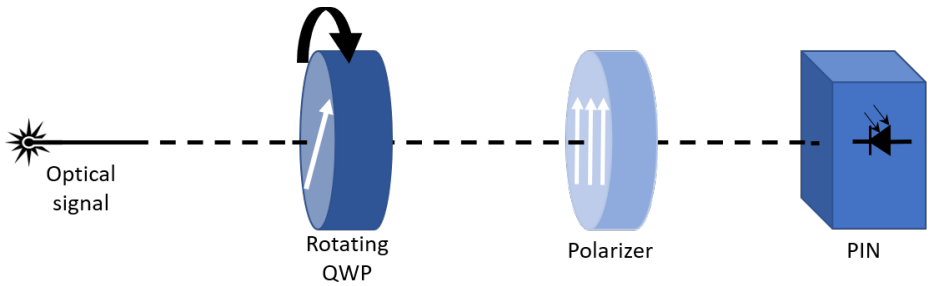

Figure 3.1: Representative scheme of the polarimeter, where the input signal focuses on the rotating QWP, then on the LP, and lastly on the PIN.

Waveplates

In practice, a waveplate is a crystalline material placed in the path of the light, inducing an additional phase shift between the two orthogonal components of the optical field, as schematically shown in Fig. 3.2. The crystal is cut so that its surface is parallel to the optic axis (axis for which the light does not suffer birefringence [51]). The component of the electric field that is aligned with the optical axis will travel with a different velocity than the perpendicular component, due to the difference between the refractive indexes.

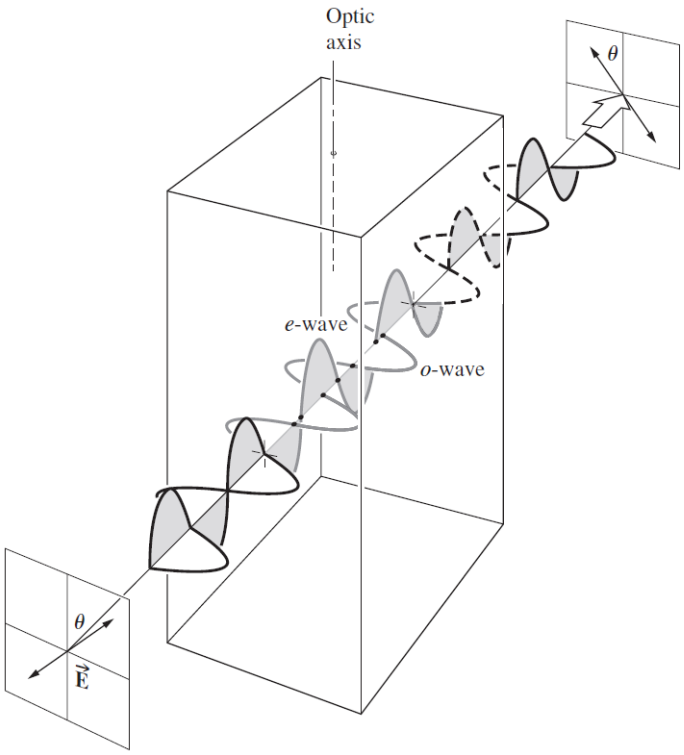

Figure 3.2: Schematic representation of the operation principle of a waveplate. A linear diagonal polarized signal passes through the crystalline material that delays one of the components of the signal in relation to the other component. The figure represents a Half Waveplate (HWP) as one of the components of the signal is delayed by $\lambda_0/2$ (π radians) with respect to the other, making the output signal polarization to be linear anti-diagonal. Adapted from [51].

The final phase difference, $\Delta\varphi$, between the two components depends on the width of the crystal, and the difference between the refractive indices [34, 52]:

$$\Delta\varphi = \frac{2\pi}{\lambda_0} d\Delta n, \tag{3.1}$$

where λ_0 is the vacuum wavelength, d is the thickness of the medium, and Δn is the difference between the refractive indices, which can be defined as $\Delta n = |n_o - n_e|$, with n_o and n_e standing for the ordinary and extraordinary refractive indices, respectively [51]. Using the definition of the optic path difference between the two components $\Lambda = d\Delta n$, equation (3.1) can be rewritten as [34, 52]:

$$\Delta\varphi = k_0 \Lambda, \tag{3.2}$$

where k_0 is the vacuum wavenumber.

In the specific case of a QWP, the resultant relative phase difference between the two components is $\Delta\varphi = \pi/2$. One can obtain that result when Λ is written in terms of wavelength fractions, such that $\Lambda = \lambda_0/m$, with $m = 4$ for a QWP. By replacing Λ by $\lambda_0/4$ in (3.2), a phase difference of $\Delta\varphi = \pi/2$ is obtained. The general waveplate matrix can be mathematically represented by the following Muller matrix:

$$\boldsymbol{M}_{\mathrm{WP}} = \begin{bmatrix} 1 & 0 & 0 & 0 \\ 0 & \cos^2 2\theta + \sin^2 2\theta \cos\phi & (1-\cos\phi)\sin 2\theta \cos 2\theta & -\sin 2\theta \sin\phi \\ 0 & (1-\cos\phi)\sin 2\theta \cos 2\theta & \sin^2 2\theta + \cos^2 2\theta \cos\phi & \cos 2\theta \sin\phi \\ 0 & \sin 2\theta \sin\phi & -\cos 2\theta \sin\phi & \cos\phi \end{bmatrix}, \tag{3.3}$$

where ϕ represents the phase retardation, and θ stands for the fast axis orientation of the waveplate.

Notice that if the QWP is rotated, the alignment of its optical axis will be changed accordingly. Such a rotating waveplate will transform a fixed input SOP into an output SOP that is continuously changing. The resulting output will focus on a polarizer, see Fig. 3.1.

Linear Polarizer

A LP is an optical device that takes a given input signal and transmits only the light that is polarized in the direction of the axis of the polarizer. An ideal polarizer transmits 100% of the light parallel to its axis, while it blocks the orthogonal polarization state. In the case of real polarizers, as they are not perfect, they can be characterized by the polarization efficiency, P [53]:

$$P = \frac{T_{\max} - T_{\min}}{T_{\max} + T_{\min}}, \tag{3.4}$$

where $T_{\max}$ and $T_{\min}$ are the maximum and minimum transmittance of a polarizer, respectively. The maximum transmittance can be obtained when a polarized light beam is focused on a polarizer with its axis parallel to the polarization of the light, while the minimum transmittance is obtained when the polarized light is perpendicular to the axis of the polarizer, as schematically shown in Fig. 3.3.

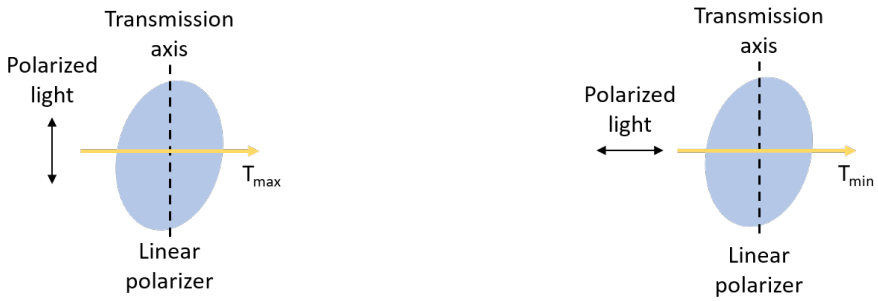

Figure 3.3: Schematic representation of the transmittance of a polarizer: (a) when the polarization of the incident light is parallel to the transmission axis of a LP the transmittance at the output is maximized; (b) when the polarization of the incident light is perpendicular to the transmission axis of a LP the transmittance at the output is minimized.

Measurement of the Stokes Parameters

The photocurrent is detected by the photodiode at the output of the polarizer, as shown in Fig. 3.1. This photocurrent is proportional to the optical power, i.e. to the square of the electric field [54]. After the detection in the photodiode, the signal is Fourier transformed, resulting in three components, a DC component, a component with the double of the rotation frequency of the rotating waveplate, and a component with the quadruple of the waveplate rotation frequency, with a phase shift [54]. For elliptical polarizations, none of the components will be zero. On the other hand, circular polarization will only produce the component with the double frequency, whereas linear polarization will only produce the component with the quadruple frequency [54]. The values of these components will be used to determine the Stokes parameters.

In the following, we describe how the mentioned components are determined and how they serve to determine the Stokes parameters. An electromagnetic wave, after passing through a waveplate, where the y-component is subjected to a retardation ϕ regarding to the x-component, and then through a polarizer, can be written as [55]:

$$E(\theta, \phi) = E_x \cos\theta + E_y e^{i\phi} \sin\theta, \tag{3.5}$$

where θ is the orientation of the linear polarizer. One can derive the intensity of the same wave as follows [55]:

$$\begin{aligned} I(\theta, \phi) &= \langle E(\theta, \phi) E^*(\theta, \phi) \rangle & (3.6)\\ &= J_{xx} \cos^2\theta + J_{yy} \sin^2\theta + J_{xy} e^{-i\phi} \cos\theta \sin\theta + J_{yx} e^{i\phi} \sin\theta \cos\theta, & (3.7) \end{aligned}$$

where $\langle E(\theta, \phi) E^*(\theta, \phi) \rangle$ denotes the time average between $E(\theta, \phi)$ and its conjugate transpose, and J_{xx}, J_{xy}, J_{yy} and J_{yx} are the elements of the following matrix [55]:

$$\boldsymbol{J} = \begin{bmatrix} \langle E_x E_x^* \rangle & \langle E_x E_y^* \rangle \\ \langle E_y E_x^* \rangle & \langle E_y E_y^* \rangle \end{bmatrix}. \tag{3.8}$$

From (3.7), it is possible to calculate the angle θ and the retardation ϕ needed to obtain the constants J_{xx}, J_{yy}, J_{xy}, and J_{yx}:

$$\begin{aligned} J_{xx} &= I(0, 0), & (3.9)\\ J_{yy} &= I(90, 0), & (3.10)\\ J_{xy} &= \frac{1}{2} \left[I(45, 0) - I(135, 0) \right] + \frac{1}{2} i \left[I(45, \pi/2) - I(135, \pi/2) \right], & (3.11)\\ J_{yx} &= \frac{1}{2} \left[I(45, 0) - I(135, 0) \right] - \frac{1}{2} i \left[I(45, \pi/2) - I(135, \pi/2) \right]. & (3.12) \end{aligned}$$

To determine J_{xx}, J_{yy}, and the real parts of J_{xy} and J_{yx}, one needs a polarizer that is properly oriented in such a way that allows transmitting the components of the azimuthal axis with $\theta = 0°$, $\theta = 45°$, $\theta = 90°$, and $\theta = 135°$. To obtain the imaginary parts of the same matrix elements the waveplate is necessary to induce a phase shift of $\lambda/4$ between the x and y components of the electric field [55].

The generic Stokes parameters, that were mentioned above in (2.14), can be written according to the previously defined constants, in (3.9) to (3.12), such that [55]:

$$\begin{aligned} S_0 &= J_{xx} + J_{yy} = I(0, 0) + I(90, 0), & (3.13)\\ S_1 &= J_{xx} - J_{yy} = I(0, 0) - I(90, 0), & (3.14)\\ S_2 &= J_{xy} + J_{yx} = I(45, 0) - I(135, 0), & (3.15)\\ S_3 &= i(J_{yx} - J_{xy}) = I(45, \pi/2) - I(135, \pi/2). & (3.16) \end{aligned}$$

When a quarter waveplate is used that can be rotated through an angle θ, the intensity of the optical beam on the detector is [56]:

$$I(\theta) = \frac{1}{2}\left[S_0 + S_1\cos^2(2\theta) + S_2\cos(2\theta)\sin(2\theta) + S_3\sin(2\theta)\right]. \tag{3.17}$$

Equation (3.17) can be rewritten using the trigonometric half-angle formulas as [56]:

$$I(\theta) = \frac{1}{2}\left[A + B\sin(2\theta) + C\cos(4\theta) + D\sin(4\theta)\right], \tag{3.18}$$

where A, B, C, and D are as follows:

$$A = S_0 + \frac{S_1}{2}, \tag{3.19}$$

$$B = S_3, \tag{3.20}$$

$$C = \frac{S_1}{2}, \tag{3.21}$$

$$D = \frac{S_2}{2}. \tag{3.22}$$

Equation (3.18) is a truncated Fourier series [56], consisting of the three components mentioned above (a DC component, a component with the double of the rotation frequency of the rotating waveplate, and a component with the quadruple of the waveplate rotation frequency, with a phase shift [54]). Following Nyquist's sampling theorem [57], eight or more data points must be taken to determine the Stokes parameters. Given that discreet intensities are measured (3.18) is rewritten as [56]:

$$I_n = \frac{1}{2} = \left[A + B\sin(2\theta_n) + C\cos(4\theta_n) + D\sin(4\theta_n)\right], \text{ with } n = 1, 2, ..., N, \tag{3.23}$$

with $N \geq 8$. The coefficients A, B, C, and D are determined from Fourier analysis, and are given by [56]:

$$A = \frac{2}{N}\sum_{n=1}^{N} I_n, \tag{3.24}$$

$$B = \frac{4}{N}\sum_{n=1}^{N} I_n\sin(2\theta_n), \tag{3.26}$$

$$C = \frac{4}{N}\sum_{n=1}^{N} I_n\cos(4\theta_n), \tag{3.25}$$

$$D = \frac{4}{N}\sum_{n=1}^{N} I_n\sin(4\theta_n). \tag{3.27}$$

For the intensity measurements, the θ intervals should be equally spaced, such that $\theta_{n+1} - \theta_n = 180°/N$. After the coefficients A, B, C, and D are measured, the Stokes parameters can be determined by the following equalities [56]:

$$S_0 = A - C, \tag{3.28}$$

$$S_1 = 2C, \tag{3.29}$$

$$S_2 = 2D, \tag{3.30}$$

$$S_3 = B. \tag{3.31}$$

Therefore, as mentioned above, the system to determine the Stokes parameters consists of a rotating QWP, a LP, and a photodiode, as shown in Fig. 3.1.

3.1.2 OTDR

An OTDR is an optoelectronic device used to characterize an optical fiber having access to just one fiber termination. In particular, it can detect and characterize discontinuities in

the fiber caused by folds, breaks, connectors, or other types of irregularities that cause the light to be scattered [58]. The operation principle of an OTDR is based on the Rayleigh scattering effect and the Fresnel reflection effect [59]. The Rayleigh scattering occurs when a light pulse, that travels along a fiber, comes across small variations of the refractive index of the fibers material. These discontinuities cause the light to scatter in all directions of space. A small portion of the light is scattered in the opposite direction of the initial light beam, this phenomenon is called Rayleigh backscattering [59].

The Fresnel reflection, on the other hand, occurs when the light beam sent through the fiber comes across abrupt changes of density in the material. These density variations can be caused by connectors or breaks that insert an air layer in the fiber. Because of these irregularities, a significant portion of the light is reflected, compared with the portion that is backscattered when the Rayleigh effect occurs. The intensity of the reflected beam is proportional to the greatness of the difference between refractive indexes, making it possible to distinguish what kind of irregularity caused the reflection or if the end of the fiber was reached by the light beam. Therefore, the portion of the light that is backscattered is detected and analyzed by the OTDR by measuring, in specific time intervals, the power of the signal, characterizing the events that occur along the fiber. The fiber length, D, can be calculated using the following expression [59]:

$$D = \frac{c}{n} \times \frac{\Delta t}{2}, \tag{3.32}$$

where c is the speed of light in vacuum, n is the refractive index of the fiber core and Δt is the time interval between the emission and the reception of the signal.

3.2 Laboratory Polarization Drift Measurements

In a first attempt to validate the polarization drift model presented in the previous chapter, we have carried out a set of measurements in the laboratory. The experimental setup used in such measurements is represented in Fig. 3.4. This setup comprises a transmitter, a receiver, and an optical channel. At the transmitter side, a laser source (model: IQ-2400, from Thorlabs) emitted a signal with a wavelength of 1550.00 nm. The signal was conducted through an optical fiber to the receiver. Two different fiber lengths were used for the optical channel, those lengths are specified in Table 3.1. At the receiver, the signal was detected by a polarimeter (model: TXP5004 with an optical head, model: PAN5710IR3, from Thorlabs), which, in turn, was connected to a computer with an acquisition software.

Measurements were obtained using one and two spans of fiber, with a total length of 80 km and 160 km. The environmental conditions of the lab were maintained as constant as possible, nevertheless, in order to change the distance and make some other adjustments to the experimental setup, given the many variables that can influence the polarization drift, it can be fallacious to make a direct comparison of the measurements.

In the experiments, we have used different sampling periods (time between measurements: 15 and 10 min). The total acquisition time was adjusted according to the speed of the polarization drift. As the drift is faster for longer fiber lengths, we used shorter total acquisition times for the longer fiber links. The measurements performed with the different parameters are discriminated in Table 3.1. Using the Stokes parameters provided by the polarimeter, we have computed the Autocorrelation Function (ACF) following the method presented in Sec. 2.3.3 in order to obtain the polarization linewidth. Due to software incompatibilities, the polarimeter had several flaws that caused him to skip some measurements, i.e. during the total period of measurements, the Stokes parameters were not measured

at certain instants of time. In this regard, we have developed a *Matlab* algorithm in order to correct these lacks, estimating the values of the Stokes parameters of the missing measurements. The algorithm used the function *interp1*, with *spline* interpolation. This interpolation method is based on a cubic interpolation that uses various values at neighboring grid points in each respective dimension.

The time evolution of the measured Stokes parameters is represented on the Poincaré sphere in Fig. 3.5, for the 80 and 160 km optical links. In the figure, the first column corresponds to the measurements using the 80 km optical link, with a sampling period of 15 min, the second column corresponds to the 160 km optical link, with a sampling period of 15 min, and the last column corresponds also to the 160 km fiber link, but with a sampling period of 10 min. The ACF and the respective fit, obtained using (2.47), are plotted in the third line of each column of Fig. 3.5.

The Stokes parameters represented in the first line of Fig. 3.5 show a noticeable drift increase with the increase of fiber link length. Such polarization drift increase is also visible in the second line, where the Stokes parameters are represented on the Poincaré sphere. The ACF function, shown in the third line of Fig. 3.5, presents a faster fall for higher fiber lengths. Longer fibers increase the speed of the ACF fall given that the longer the fiber is, the greater will be its exposure to environmental perturbations that cause the random polarization drift due to the birefringence mechanisms discussed in Sec. 2.3.1.

Table 3.1: SOP laboratory measurement parameters used for the several fiber lengths and the respective Δp results.

Fiber length (km)	Sampling period (min)	Wavelength (nm)	Total acquisition time (days)	Δp (s^{-1})
80	15	1553.33	3.9	1.7×10^{-6}
160	15	1553.33	2.7	3.5×10^{-6}
160	10	1550.00	2.6	5.7×10^{-6}

Table 3.1 contains the various Δp values obtained from the lab measurements. Consid-

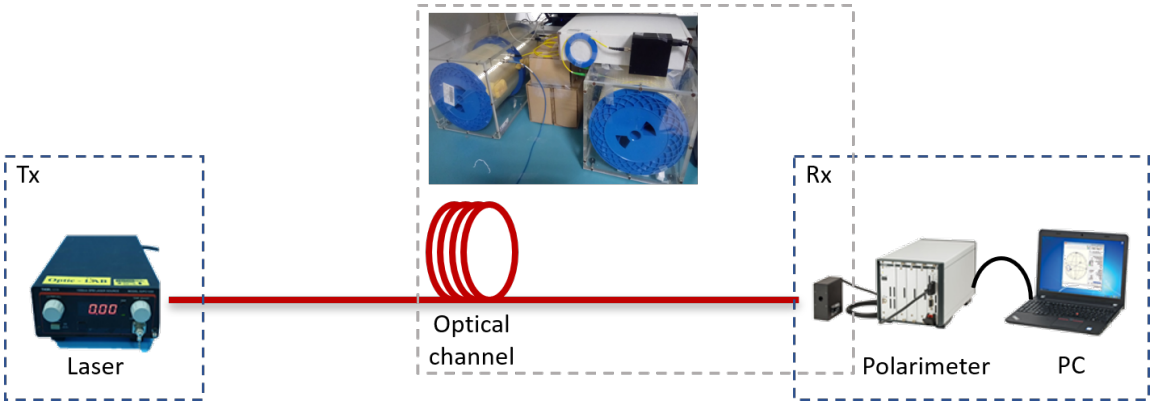

Figure 3.4: Schematic diagram of the setup used to measure the SOP drift. The transmitter (Tx) is comprised by the laser that sends an optical signal through the optical channel to the receiver (Rx). At the receiver, the optical head of the polarimeter detects the signal. The polarimeter is connected to a computer with the polarimeter acquisition software. The inset shows the fiber coil used in the laboratory measurements, as well as the optical head of the polarimeter.

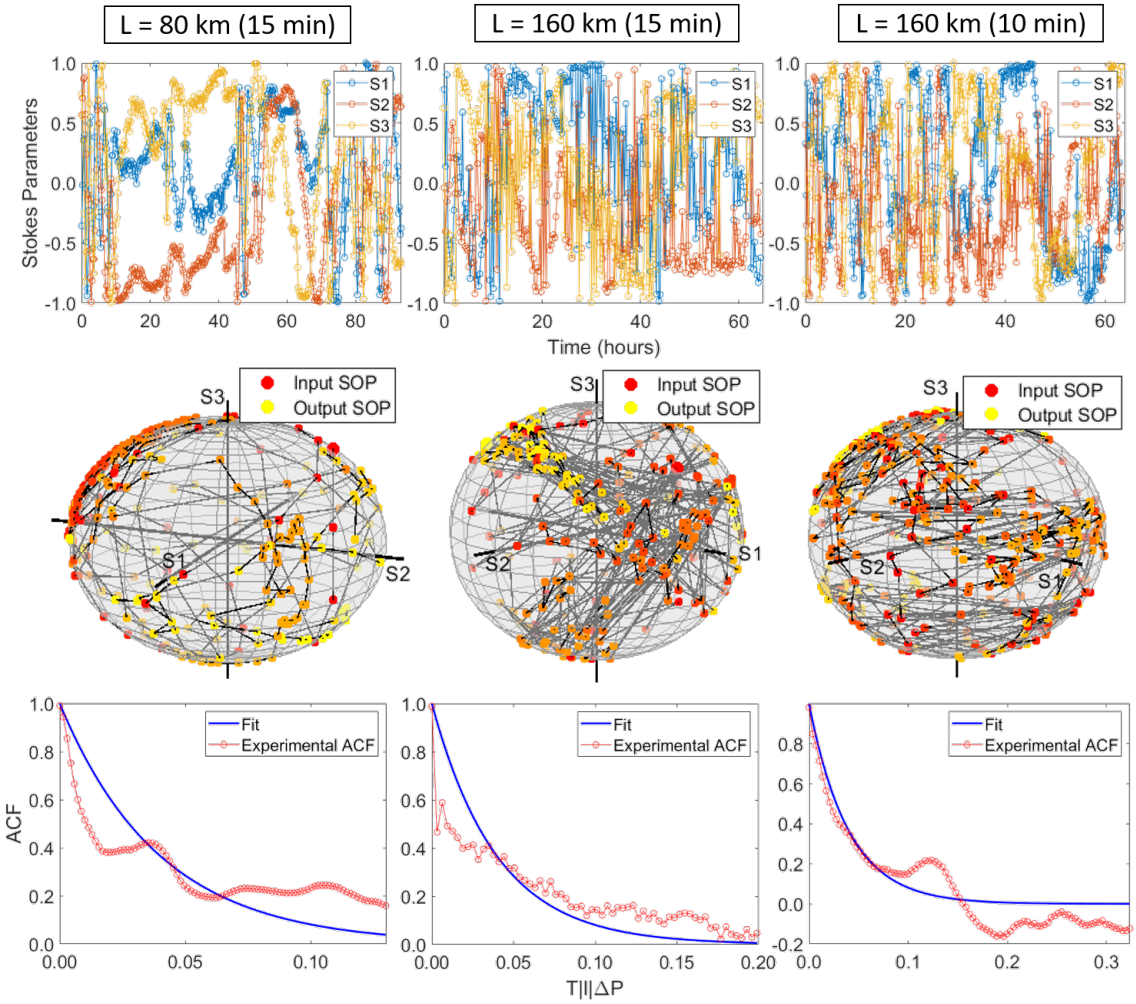

Figure 3.5: Results of the laboratory measurements of the Stokes parameters. The first and second lines show a two and three-dimensional representation of the Stokes parameters, respectively, and the third line shows the estimated ACF curve and the respective fit obtained with (2.47). The first column corresponds to a 80 km fiber link with a sampling period (T) of 15 min, the second column corresponds to a 160 km fiber link with a sampling period of 15 min, and the third column also corresponds to a 160 km fiber link, however, with a sampling period of 10 min.

ering that these measurements were done in the same environmental conditions, one can conclude that fiber-optic length influences the properties of the SOP time drift. An increase in length causes a decrease in correlation between the SOPs, given that the Δp obtained for the 80 km optical link is smaller than the Δp obtained for the 160 km optical link. The two Δp obtained for the same length can be explained by some variation of the environmental perturbations.

3.3 In-Field Polarization Drift Measurements

The characterization of the SOP time drift was also performed in two in-field experiments. The first one was carried out in the city of Aveiro, where an optical loop was established between the Instituto de Telecomunicações building and an Altice Labs datacenter (via

CTT-Aveiro). To establish this link, four parallel dark fibers connecting the two buildings were properly interconnected (see Fig. 3.6). The second in-field experiment was carried out in Lisbon, using a dark fiber connecting two sites belonging to the national public administration. This experiment was developed in the context of a collaboration between the Instituto de Telecomunicações and the Portuguese Ministry of National Defence to design a framework envisioning the establishment of QKD-enabled secure links in Lisbon.

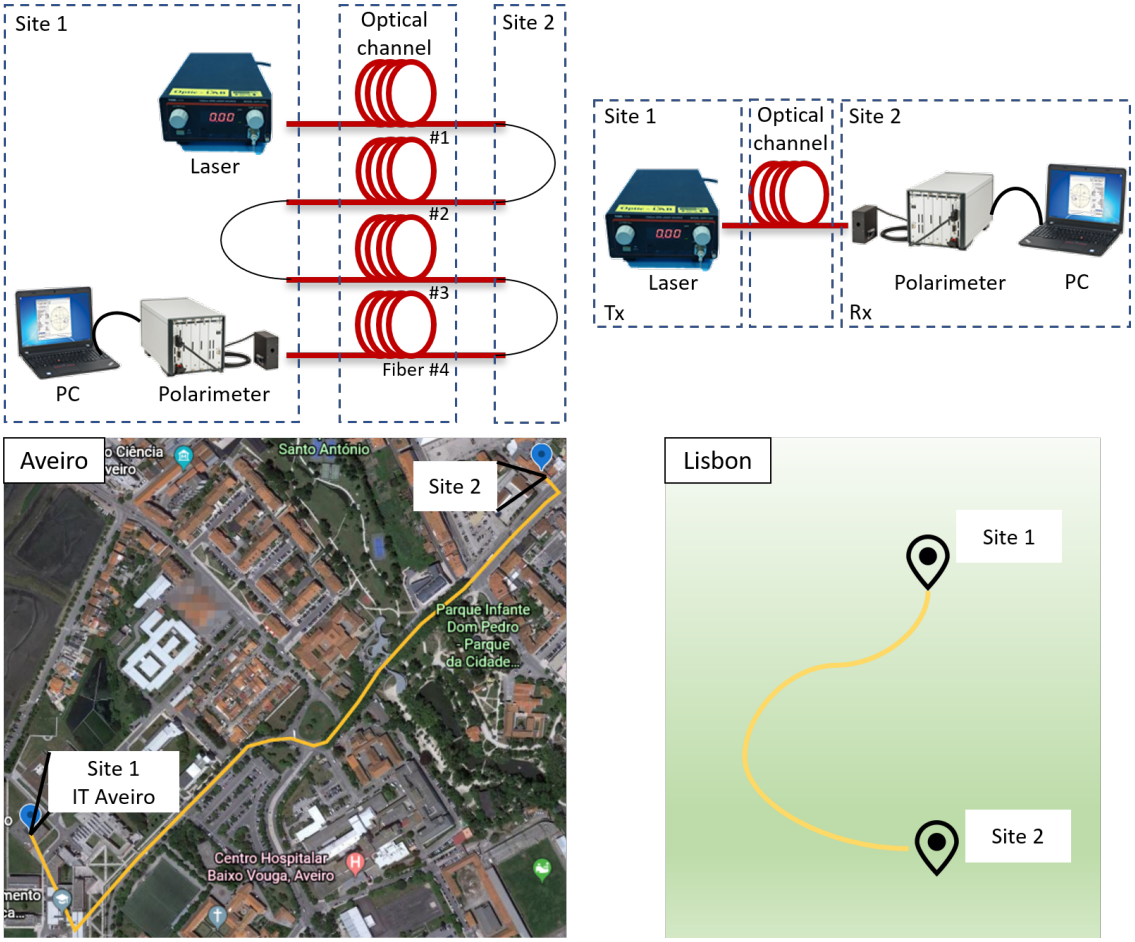

Figure 3.6: Schematic representation of the setup used for the field measurements. The optical link used in Aveiro comprised two optical loops, with the transmitter and the receiver located at the same site (IT Aveiro), as shown in the map. In the Lisbon measurements, the link was comprised by a single fiber connecting two sites belonging to the national public administration.

In the case of the Aveiro field measurements, as the exact length of the optical links was unknown, it was necessary to perform measurements with an OTDR (model: AXS-100 from EXFO), explained in Section 3.1.2, to determine the length of the tested fibers and consequently the total length of the established optical loop. The results obtained with the OTDR are shown in Fig. 3.7. First, we measured the link length for only one round trip, and after we measured the link length for two round trips. In Fig. 3.7, the green and red lines represent the measurements for just one round trip, and the blue line represents the measurements for two round trips. The measurements were performed with an optical pulse larger than the optimal pulse width, however, the only parameter of interest was the length of the optical link. From the results shown in Fig. 3.7, we can conclude that the optical link

had a total length of 6.6 km. For the Lisbon setup, the length of the optical link was a known parameter, 3.1 km.

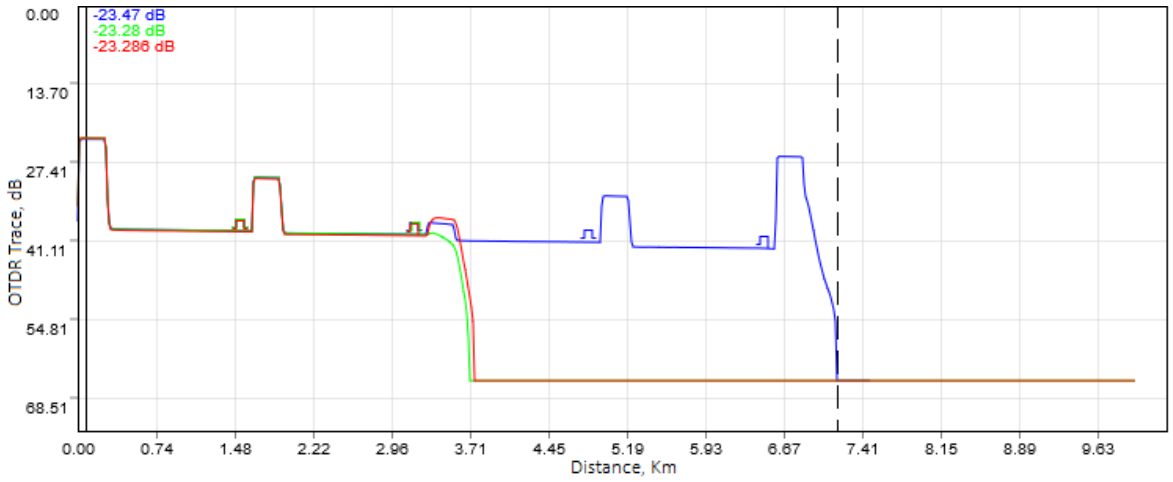

Figure 3.7: Graph obtained with the OTDR to determine the exact length of the used optical link in Aveiro city. The green line represents the result of the measurement of one of the loops, the red line is the second loop and the blue line represents the measurement of both loops together.

The parameters used for the field measurements are discriminated in Table 3.2. The Stokes parameters measured in Aveiro and Lisbon, are represented on the Poincaré sphere, in Fig. 3.8, where the first column corresponds to the measurements made in Aveiro, and the second column corresponds to the measurements performed in Lisbon. The first and second lines show the two- and three-dimensional representation of the Stokes parameters, respectively, while the third line shows the estimated ACF curve and the respective fit, obtained with (2.47).

The problem caused by software incompatibilities that lead the polarimeter to skip some measurements was solved with the solution presented in Sec. 3.2, i.e. using a *Matlab* script to estimate the value of the skipped measurements. The values obtained for the Δp parameter in the field measurements are also presented in Table 3.2.

Table 3.2: SOP field measurement parameters used for the several fiber lengths and the respective Δp values.

Fiber length (km)	Sampling period (min)	Wavelength (nm)	Total acquisition time (days)	Δp (s^{-1})
3.1 (Lisbon)	10	1550.00	6.9	1.1×10^{-8}
6.6 (Aveiro)	10	1550.00	4.8	8.1×10^{-9}

Results show a smaller value for the Δp parameter in the Aveiro measurements, meaning that this optical link exhibits the highest correlation between the SOPs, i.e. and consequently a slower time drift. This corresponds to what is observed in the first column of Fig. 3.8, where it is possible to see that the Stokes parameters remain almost constant with time. The ACF also shows a slow decrease, reflecting that the correlation between subsequent Stokes parameters is high. These results may be due to the location of the fiber, as it is underground, the environmental perturbations are minimal.

The value obtained for the Δp parameter in the Lisbon measurements is slightly higher than the one obtained in Aveiro, but much smaller when compared with the ones obtained in

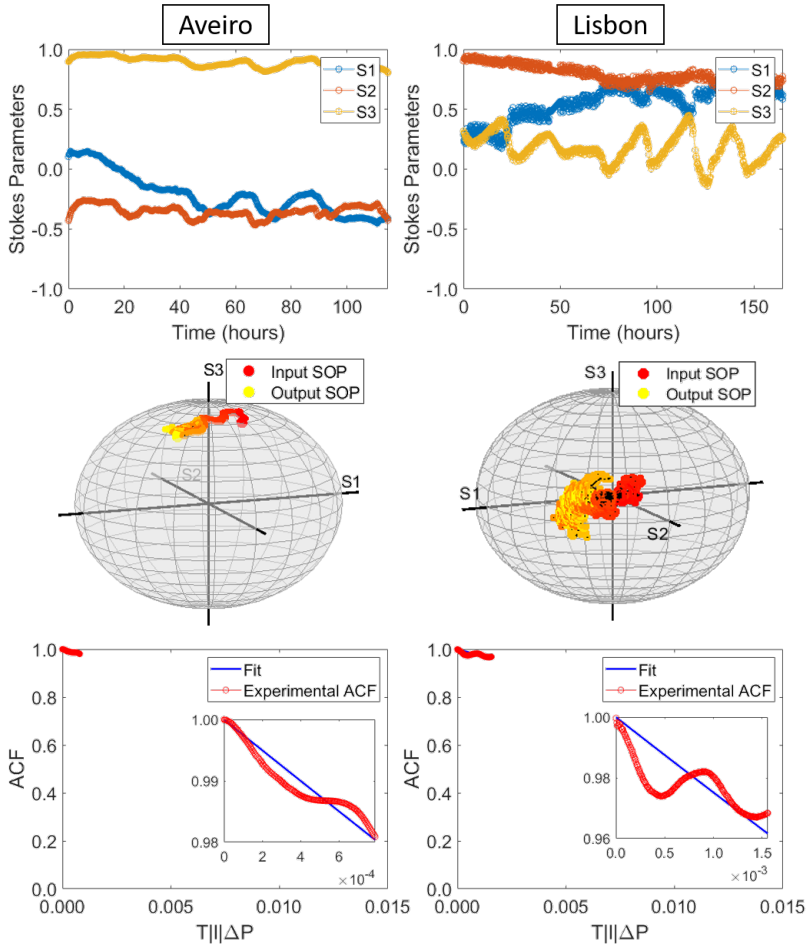

Figure 3.8: Result of the field measurements of the Stokes parameters. The first and second lines show a two- and three-dimensional representation of the Stokes parameters, respectively, and the third line shows the estimated ACF curve and the respective fit obtained with (2.47). The first column corresponds to the measurements made in Lisbon (3.1 km), while the second column corresponds to the measurements made in Aveiro (6.6 km). The measurements in both locations were done with a sampling period of 10 min. A complete list of the measurement parameters are presented in Table 3.2.

the lab. On the other hand, the Lisbon measurements show very-high frequency oscillations (second column of Fig. 3.8) that were not observed in the Aveiro measurements. The origin of these oscillations is related to the positioning of the optical head of the polarimeter, which was placed in an environment that had some working vibrating device. This conclusion was taken after a short measurement was made at the same position of the previously taken data and then away from any possibly vibrating devices, we concluded that the oscillation was, in fact, due to the polarimeters optical head location. Removing these oscillations, the Stokes parameters present few variations with time, leading to a small decrease of the ACF, as can be seen in the second column and third line of Fig. 3.8.

Chapter 4

Polarization Encoding for QKD

As polarization-encoded Quantum Key Distribution (QKD) systems have shown promising results, the need to develop time-efficient and stable polarization encoding and decoding units has increased. The encoding units would consist of a system that can easily generate the necessary State of Polarization (SOP) to encode the qubits. Therefore, this chapter is dedicated to polarization control, namely to develop a method that allows to generate and send a specific SOP through an optical fiber.

The first section discusses the polarization controller properties, detailing the operation principle of the polarization controller used in this dissertation. The next section proposes a new method to generate four SOPs. Then, the experimental assessment and results of the developed method are presented. Lastly, the developed method is integrated into a QKD system in order to validate it performance in a realistic scenario.

4.1 Electronic Polarization Controller (EPC)

Polarization controllers are optical devices that allow changing an arbitrary input SOP of an optical beam into any desired output SOP. There are several polarization control devices based on electro-optic crystals [60], rotational phase plates [61], electromagnetic fiber squeezers [62], Faraday rotators [63], fiber-coil based devices [64, 65], among others. In laboratories, the most used polarization control devices are the fiber-coil based ones [65], which typically comprise three waveplates and whose orientation angles are adjusted manually.

When an optical fiber is submitted to mechanical stress, its length varies, hence, the refractive index changes. This phenomenon is called the elasto-optic effect. Most polarization control schemes use the elasto-optic properties of silica, regulating the polarization by squeezing the fiber [62, 66], or by bending it [64] in a controlled way.

In this dissertation, an Electronic Polarization Controller (EPC) (model: PolaRITE III, from General Photonics) is used to deterministically generate different deterministic SOPs. This EPC comprises four waveplates inline to change polarization by squeezing the fiber, see Fig. 4.1. In this case, the fiber squeezing mechanism includes a piezoelectric material, to which a voltage is applied. The pressure applied on the fiber is proportional to that voltage, meaning that by applying a voltage to the waveplate, the fiber is squeezed and the refractive index in one direction of the fiber changes. The four waveplates of the EPC are arranged so that the fast axis of the second and the fourth waveplate are oriented 45° relatively to the fast axis of the first and third waveplate, as schematically shown in Fig. 4.1.

The EPC, composed of four waveplates, can be mathematically described by the matrix

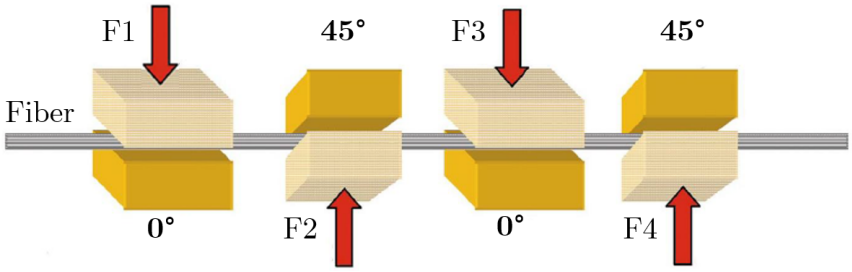

Figure 4.1: Schematic representation of the EPC, where the blocks represent the waveplates, being that the fast axis of the second and fourth ones are oriented at 45° relatively to the first and third ones. Adapted from [67].

$\boldsymbol{M}_{\text{EPC}}(V_1, V_2, V_3, V_4)$, which results from the product of the individual waveplate matrices as a function to the voltage applied on each of them [68]:

$$\boldsymbol{M}_{\text{EPC}}(V_1, V_2, V_3, V_4) = \boldsymbol{M}_{45}(V_4)\boldsymbol{M}_0(V_3)\boldsymbol{M}_{45}(V_2)\boldsymbol{M}_0(V_1), \tag{4.1}$$

where $\boldsymbol{M}_0(V_i)$, with $i = 1, 3$, and $\boldsymbol{M}_{45}(V_j)$, with $j = 2, 4$, are the matrices that represent the waveplates that are oriented at 0° and at 45°, respectively. The voltages V_1, V_2, V_3 and V_4 can be expressed in terms of the retardation phase, ϕ, of each waveplate. The conversion is done using the following equation:

$$V = \frac{\phi \cdot V_\pi}{\pi}, \tag{4.2}$$

where V_π is the half-wave voltage, that is, the voltage required to induce a change of 180° between the phase of two orthogonally polarized light waves. When representing the SOP in the Stokes space, this voltage makes a particular SOP to rotate half a circle on the Poincaré sphere. The matrices $\boldsymbol{M}_0(\phi)$ and $\boldsymbol{M}_{45}(\phi)$ can be obtained from (3.3) by using $\theta = 0°$ and $\theta = 45°$, respectively [27]:

$$\boldsymbol{M}_0(\phi) = \begin{pmatrix} 1 & 0 & 0 & 0 \\ 0 & 1 & 0 & 0 \\ 0 & 0 & \cos\phi & -\sin\phi \\ 0 & 0 & \sin\phi & \cos\phi \end{pmatrix}, \tag{4.3}$$

$$\boldsymbol{M}_{45}(\phi) = \begin{pmatrix} 1 & 0 & 0 & 0 \\ 0 & \cos\phi & 0 & \sin\phi \\ 0 & 0 & 1 & 0 \\ 0 & -\sin\phi & 0 & \cos\phi \end{pmatrix}, \tag{4.4}$$

where ϕ is the retardation phase of the waveplate (the same as in (4.2)). The EPC matrix, represented by (4.1), establishes the relationship between the input and output SOPs, as follows:

$$\mathbf{S}_{\text{out}} = \boldsymbol{M}_{\text{EPC}}(V_1, V_2, V_3, V_4)\mathbf{S}_{\text{in}}, \tag{4.5}$$

where $\mathbf{S}_{\text{in}}$ is the input SOP and $\mathbf{S}_{\text{out}}$ is the output SOP.

4.1.1 EPC Characterization Setup

In order to develop a method capable of generating different deterministic SOP, it is important to perform a full characterization of the EPC. In particular, it is crucial to assess the linearity between the induced phase and the applied voltage. This characterization of the EPC should determine the equation that best fits the response between the two parameters.

The setup used to characterize the EPC in terms of its response to the applied voltage is shown in Fig. 4.2. After the EPC, a 50/50 Beam Splitter (BS) divides the power of the optical signal by two, so that we have a monitor signal at one output of the BS and the other output allows the signal to follow to the QKD quantum channel, as shown further in Sec. 4.4. This component does not affect the polarization, reducing the optical power to half of the initial value. After the BS, a PBS divides the incoming optical signal into its horizontal and vertical polarization components. The arm that carries the horizontally polarized photons is then guided to a p-i-n Photodiode (PIN) that converts the optical power into a voltage. Since the voltage values applied on the four waveplates of the EPC induce a certain rotation in its output SOP, the polarization components aligned with the principal axes of the PBS will change their magnitudes. This, in turn, will change the optical power in each arm of the PBS and consequently the electric signal at the output of the PIN. Notice that the performed characterization would also be possible by using a Linear Polarizer (LP) instead of a PBS (which in practice acts as two LPs rotated at 90°).

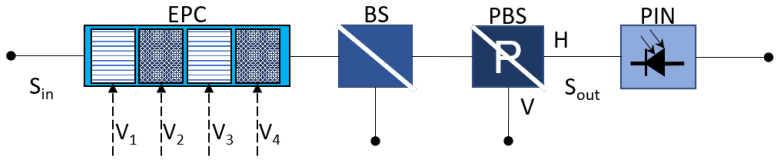

Figure 4.2: Schematic representation of the setup used to characterize the EPC.

4.1.2 Characterization Setup Modeling

A theoretical analysis was performed by considering the mathematical representation of the different components that integrate the setup used for the EPC characterization. In this analysis, we assumed that only the second 45° oriented waveplate of the EPC is actuated (with a voltage V_4) in order to change the output SOP. After the EPC, we used a 50/50 BS to divide the power of the main optical signal by two, where one of the outputs of the BS follows the quantum channel and the other follows to the PBS to the SOP monitoring setup. The PBS divides the main signal into two orthogonal polarization components (H and V), and the output corresponding to the horizontal polarization follows to a PIN. The matrix of the horizontal output of the PBS is as follows [69]:

$$\boldsymbol{M}_{\mathrm{PBS}} = \frac{1}{2}\begin{pmatrix} 1 & 1 & 0 & 0 \\ 1 & 1 & 0 & 0 \\ 0 & 0 & 0 & 0 \\ 0 & 0 & 0 & 0 \end{pmatrix}. \tag{4.6}$$

Using (4.6) and (4.1), the SOP at the horizontal output of the PBS can be written as follows:

$$\mathbf{S}_{\text{out}} = \boldsymbol{M}_{\text{PBS}}\boldsymbol{M}_{\text{EPC}}(0,0,0,V_4)\mathbf{S}_{\text{in}} = \frac{1}{4}\begin{pmatrix} S_{\text{in},0} + S_{\text{in},1}\cos(\frac{V_4\cdot\pi}{V_\pi}) + S_{\text{in},3}\sin(\frac{V_4\cdot\pi}{V_\pi}) \\ S_{\text{in},0} + S_{\text{in},1}\cos(\frac{V_4\cdot\pi}{V_\pi}) + S_{\text{in},3}\sin(\frac{V_4\cdot\pi}{V_\pi}) \\ 0 \\ 0 \end{pmatrix}. \tag{4.7}$$

In the previous equation, the 1/4 factor consists out of two 1/2 factors, one that corresponds to the PBS matrix, and the other corresponding to the BS effect on the intensity of the optical signal. As the PIN only measures the intensity of the optical signal, the Stokes parameter S_0 is used to represent the evolution intensity at the output of the PBS:

$$S_{\text{out},0} = S_{\text{in},0} + S_{\text{in},1}\cos\left(\frac{V_4\cdot\pi}{V_\pi}\right) + S_{\text{in},3}\sin\left(\frac{V_4\cdot\pi}{V_\pi}\right). \tag{4.8}$$

Equation (4.8) can therefore be used to test the EPC waveplate behavior, namely by comparing it with experimental data obtained with the setup represented in Fig. 4.2.

4.1.3 Characterization Results

To understand the behavior of the EPC, (4.8) was fitted to the experimental data, see Fig. 4.3. The experimental data was obtained applying a voltage range of $[0-4]$ V to the fourth waveplate of the EPC, using a step voltage of 0.01 V.

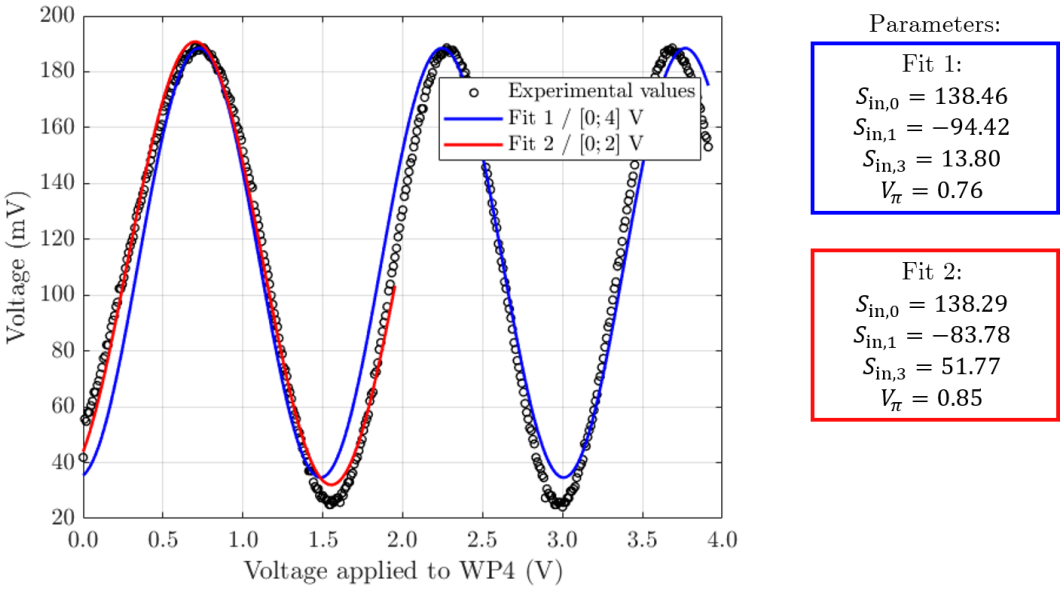

Figure 4.3: Voltage received at the PIN as a function of the voltage applied on the fourth waveplate (V_4) of the EPC. Two fits were made, one for a voltage range applied on the fourth waveplate from 0 to 4 V (Fit 1) and the other with a voltage range from 0 to 2 V (Fit 2). The fitting was made using (4.8). The parameters of (4.8) obtained for each fit are also presented.

For a voltage range of $[0-4]$ V, we observe a mismatch between the experimental data and the theoretical model (Fit 1) for certain sub-ranges of voltages V_4, see Fig. 4.3. However, if the fitting range is reduced to $[0-2]$ V, a better result is obtained (Fit 2). This leads to the conclusion that the response of the EPC waveplate is not linear for large voltage ranges.

Due to the PBS placed right before the PIN, the values received by the PIN are a projection of the S_1 axis, as mentioned before. Therefore, a step-by-step increasing voltage applied on one of the waveplates should result in a sine function with a defined period, measured by the PIN. However, it was noticed that the measured curves do not present a constant period, given that the curves show different curve apertures, most noticeable between the first and the second maxima. This can be seen in Fig. 4.4. This lack of reproducibility can be related to the fact that the used EPC uses piezoelectric materials. These materials might not apply a linear pressure on the fiber as already mentioned.

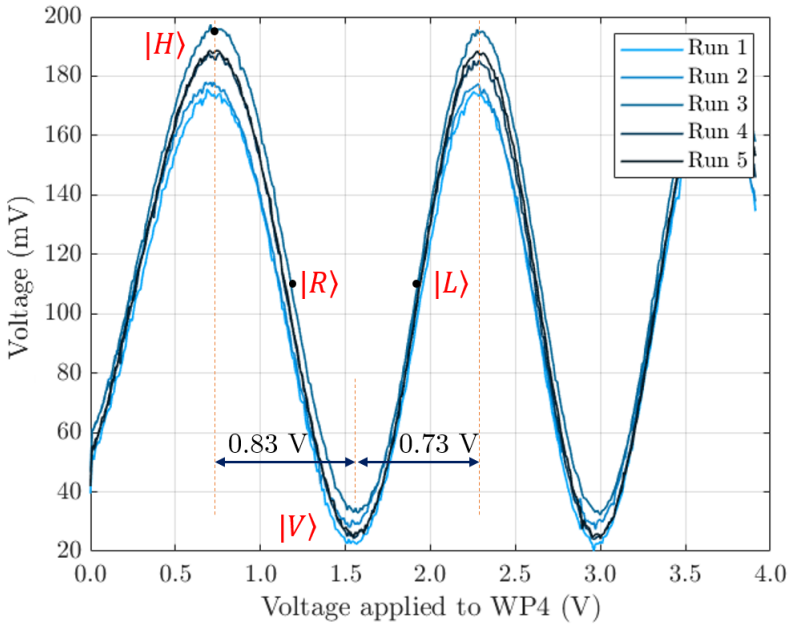

Figure 4.4: Experimental results for the fourth waveplate characterization. The graph shows the optical power received by the PIN as a function of the voltage applied to the fourth waveplate. Five runs were made in the same conditions to assess the reproducibility of the system. The points represented in the figure, referred to as $|H\rangle$, $|R\rangle$, $|V\rangle$, and $|L\rangle$, correspond to the horizontal, right-hand circular, vertical, and left-hand circular SOP, respectively.

From the results shown in Fig. 4.4, it is possible to conclude that two different values of V_π should be considered given the poor linearity of the EPC. For the first three polarization states (horizontal, right-hand circular, and vertical) a V_π of 0.83 V should be used, while for the last state (left-hand circular) a smaller value should be used: about 0.73 V.

After this characterization, the theoretical model of how to generate the four output SOPs will be explained in detail in further subsections.

4.2 SOP Generation Method

As mentioned previously, the EPC must be able to generate four different SOPs in order to be integrated into a QKD polarization-encoding sub-system. The four SOPs should form two non-orthogonal bases, with each base defined by two orthogonal SOPs. One of those states is used to encode a "0" and the other a "1". In order to efficiently obtain those four states, we developed an algorithm to automatically compute the required voltages to be applied to the EPC waveplates. This way, the four output SOPs can be written as a function of four voltages, one for each waveplate:

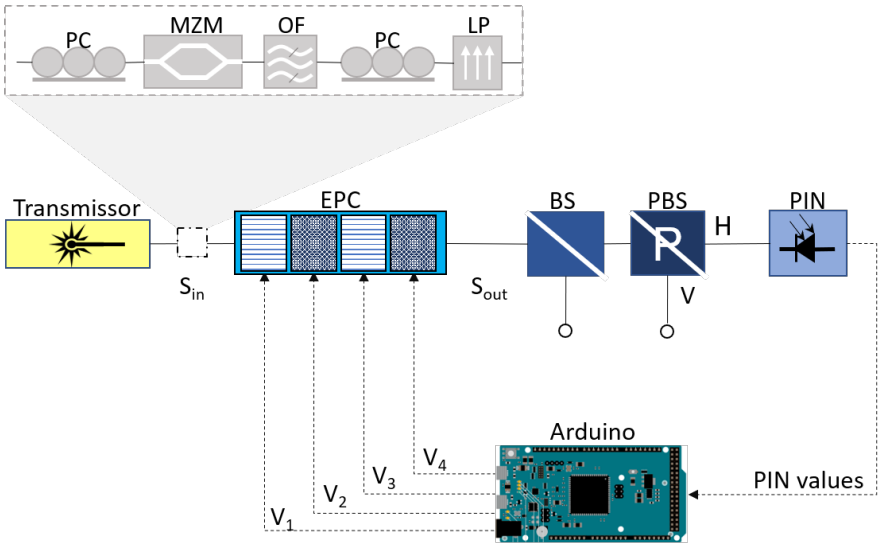

Figure 4.5: Schematic representation of the experimental setup used to deterministically generate four SOPs with an EPC. $\mathbf{S}_{\text{in}}$ and $\mathbf{S}_{\text{out}}$ are the input and output signals, respectively, and V_i is the voltage that the Arduino sends to the waveplate i.

$$\mathbf{S}_{\text{out},j} = \boldsymbol{M}_{\text{EPC}}(V_{1,j}, V_{2,j}, V_{3,j}, V_{4,j})\mathbf{S}_{\text{in}}, \tag{4.9}$$

where $V_{i,j}$, with $i = 1, ..., 4$, are the voltages applied to the waveplates in order to obtain the output SOP $\mathbf{S}_{\text{out},j}$, that can be written in terms of angles, as described by (4.2). The algorithm assumes a feedback system where the PIN voltage is used to control the EPC, as shown in Fig. 4.5.

The operation principle of the setup used to generate the four output SOPs starts by sending an optical signal; in the implementation, we used a tunable laser source, with a wavelength of 1547.72 nm. The signal SOP at the output of the laser is tuned by a manual PC before entering in the Mach-Zehnder Modulator (MZM), which is operated as a amplitude modulator in order to generate a pulsed signal. At the MZM output, an Optical Filter (OF) is used to eliminate the optical noise from the laser. Then, the optical signal passes through another PC and a LP to ensure that the signal that enters the EPC has a known, deterministic, and stable polarization. After that, the signal enters the EPC. After the EPC, the optical signal passes through a 50/50 BS that divides the signal into two arms. One of the arms of the BS leads to the polarization control setup that includes a PBS. The PBS separates the horizontally polarized photons from the vertically polarized ones. One of those output beams, of the PBS, is guided to a PIN. The PIN converts the optical signal into an electrical signal, which is sent to an Arduino Due. The Arduino Due runs the proposed algorithm that computes the values received from the PIN to generate the voltages to be applied on the EPC.

Notice that the waveplates with different orientation angles cause different rotations of the SOP on the Poincaré sphere. By applying a voltage on the first or third waveplate (oriented at 0°) causes a rotation of the SOP around the S_1 axis, while applying it on the second or fourth waveplate (oriented at 45°) causes a rotation around the S_2 axis, as shown in Fig. 4.6a [70]. This property can be explored to transform an arbitrary input SOP into any desired output SOP. In the light of this, the four different SOPs will be generated using the combination of those two types of waveplates. In a first stage, no voltage is applied to the first three waveplates, while a step voltage is applied on the fourth waveplate so that the SOP, step-by-step, makes one complete turn around the S_2 axis of the Poincaré sphere. In

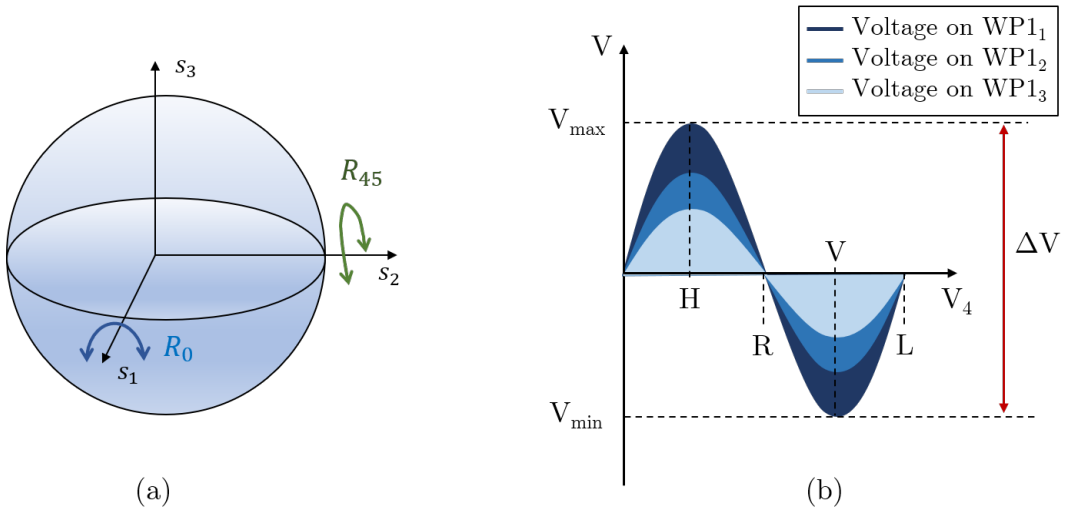

Figure 4.6: (a) Schematic representation of the Poincaré sphere rotations induced when voltages are applied to the two types of waveplates (oriented at 0 and 45°) of the EPC [70]. (b) Schematic representation of the curves that are obtained from the PIN as a function of the voltage, V_4, applied on the fourth waveplate. Each curve is obtained for a particular voltage, V_1, applied on the first waveplate. The maximum amplitude curve is used to calculate the voltages needed for each SOP to be generated.

each step, the voltage received from the PIN is registered by an Arduino Due. The array of values registered by the Arduino will result in a sinusoidal curve. Using such information, the algorithm computes the maximum and the minimum values of that curve in order to calculate the total voltage difference, ΔV, i.e. the amplitude of the curve representing the PIN voltage as a function of the voltage applied to the fourth waveplate, as shown in Fig. 4.6b.

In the next stage, the voltage applied to the first waveplate is increased by a small step, and then the fourth waveplate is again actuated making the SOP do a complete turn around the S_2 axis. Again, the values are registered in each step so the second ΔV is calculated. Notice that the goal is to maximize the value of ΔV.

After the third iteration, where an incremented value of voltage was applied to the first waveplate and a third ΔV is determined, the three ΔVs are compared. For the cases where the ΔV is decreasing, increasing or if a minimum is reached, the algorithm continues, until a maximum is found. If a maximum is found, the voltage applied to the first waveplate is not increased anymore. When the ΔV converges to the maximum voltage that means that the SOP has reached the S_1OS_3 plane, defined by the black dots in Fig. 4.7. After this, the maximum and minimum of the array obtained from the PIN are computed. The applied voltage leading to a maximum value at the PIN output will correspond to the point $(1, 0, 0)$ on the Poincaré sphere, i.e. the horizontal polarization state. Similarly, the applied voltage that leads to a minimum value at the PIN output corresponds to the point $(-1, 0, 0)$ on the Poincaré sphere, i.e. the vertical polarization state. From the voltage values found to generate the horizontal and vertical states, we can easily determine the voltages to generate the right- and left-hand circular states. The midpoint between the voltage that induces the horizontal state and the voltage that induces the vertical state corresponds to the voltage that induces the right circular polarization, represented by the point $(0, 0, 1)$ on the Poincaré sphere. Likewise, the voltage that induces the left circular polarization state (point $(0, 0, -1)$ on the Poincaré sphere), is obtained by calculating the midpoint between the voltage that induces the vertical state and the voltage that induces the horizontal state. These four states

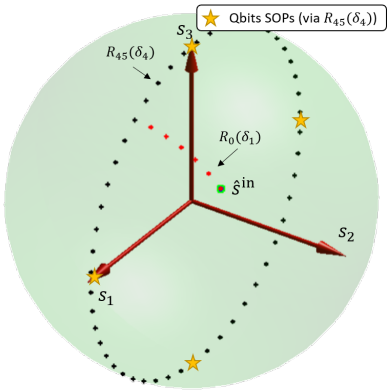

Figure 4.7: Schematic representation of the SOP rotations used by the algorithm to determine the voltages to generate four output SOPs. Voltage is applied to the first waveplate in order to rotate the SOP to the S_1OS_3 plane, with help from the fourth waveplate. After that rotation, the four output SOPs can be generated using only the fourth waveplate. Adapted from [70].

are denoted by the yellow stars in Fig. 4.7.

Notice that the V_π value corresponds to the voltage required to induce a rotation of π radians. That is, V_π is the voltage needed to change a horizontal SOP to a vertical SOP. Since this value can change due to environmental conditions, e.g. temperature, this parameter is computed every time the algorithm is executed. At this point, we must take into consideration the characterization results presented in Sec. 4.1, where we observed that the parameter V_π may present some fluctuations. In the light of this, the voltage that has to be used to generate the circular polarization state must be carefully adjusted. After this point, the algorithm can output the voltage values to be applied on each waveplate in order to generate each of the four SOPs. Although applying a set of four voltages, a constant voltage will be applied to the three first waveplates, and only the fourth waveplate is required to be actuated with different voltages along the time to generate the desired SOPs, i.e the qubits to send through the quantum channel. This way, (4.2) can be simplified:

$$\mathbf{S}_{\text{out},i} = \boldsymbol{M}_{\text{EPC}}(V_1, V_2, V_3, V_{4,i})\mathbf{S}_{\text{in}}. \tag{4.10}$$

A flowchart of the algorithm is shown in Fig. 4.8.

4.3 Experimental Assessment of the Proposed Method

The method explained in the previous section was experimentally tested with the setup shown in Fig. 4.9. First, we tested the searching process of the maximum ΔV, where an Arduino Due sent incremented values of voltage to the first waveplate. Next, the fourth waveplate sent, step-by-step, an array of voltages so that the SOP makes one turn around the S_2 axis, as shown in Fig. 4.10a.

Each curve presented in Fig. 4.10a corresponds to a particular voltage applied to the first waveplate, while every single point of the different curves corresponds to the voltage applied to the fourth waveplate. The curves show a slight side drift in relation to each other. This curve translation occurs because the referential of the EPC is not perfectly aligned with the referential of the PBS. As the ΔVs of the last two curves were not increasing anymore, the

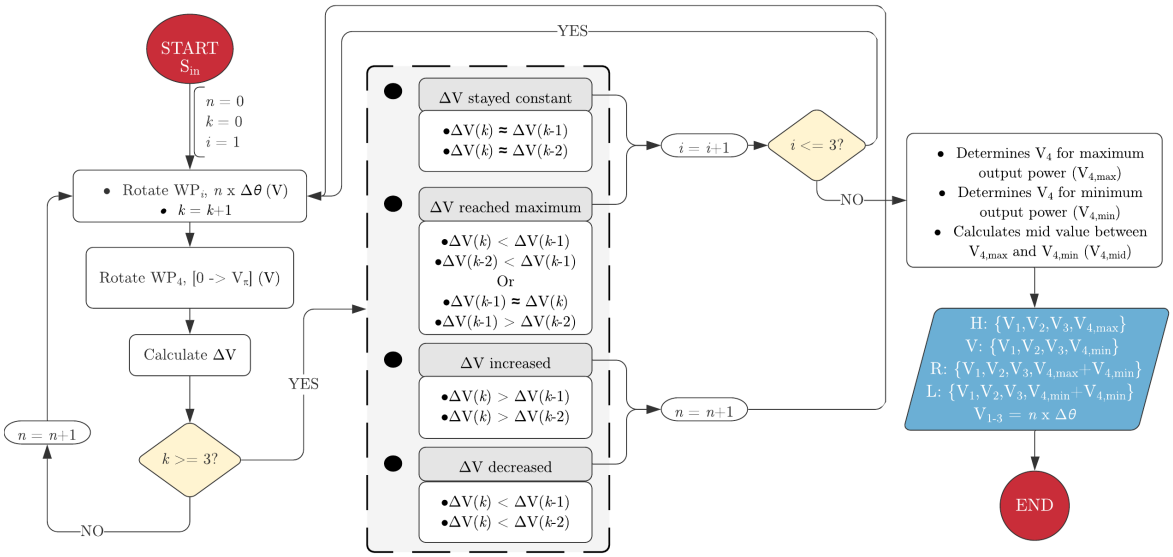

Figure 4.8: Flowchart of the algorithm (implemented in the Arduino), where i is the waveplate number, n is the index that determines the voltage applied to the waveplate, i.e. $n \times \Delta\theta$, with $\Delta\theta$ being the predefined voltage increment, and k determines if a comparison between ΔVs can be made.

algorithm stopped because the SOP reached the plane S_1OS_3 on the Poincaré sphere, see Fig. 4.10b.

Results show that there are some differences between the theoretical model presented in Sec. 4.2 and the practical implementation. For instance, the number of waveplates that was effectively used. Given that only two types of rotations are performed, one around the S_2 axis and the other around the S_1 axis, only two waveplates were used. However, using the full capacity of the EPC might decrease the total time used to output the four SOPs but

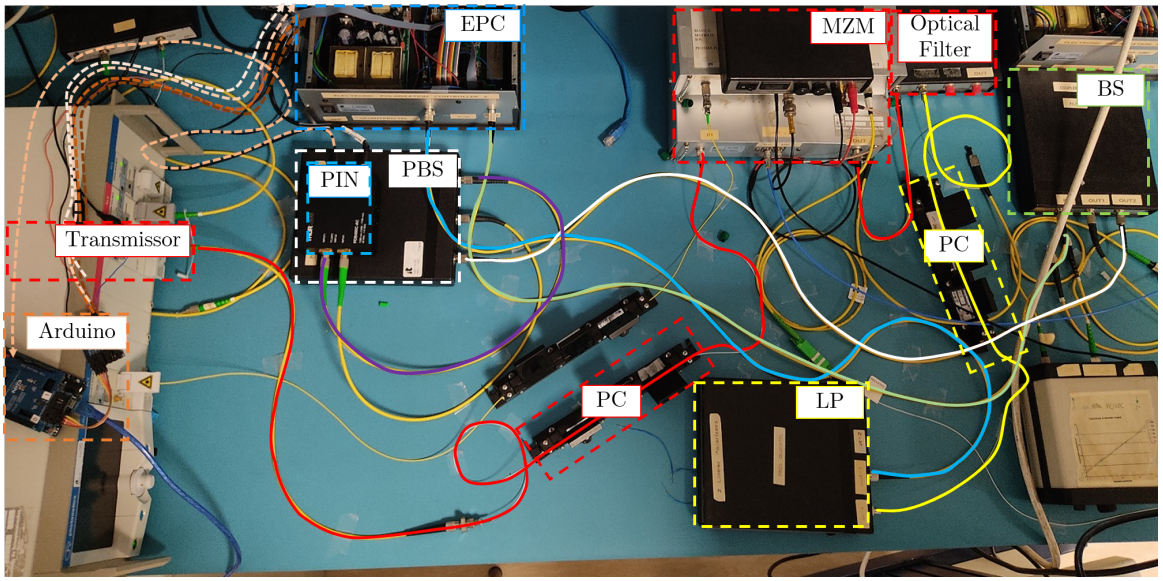

Figure 4.9: Image of the experimental setup used to test the algorithm. The colored lines describe the path of the optical (continuous lines) and electric signal (dashed lines).

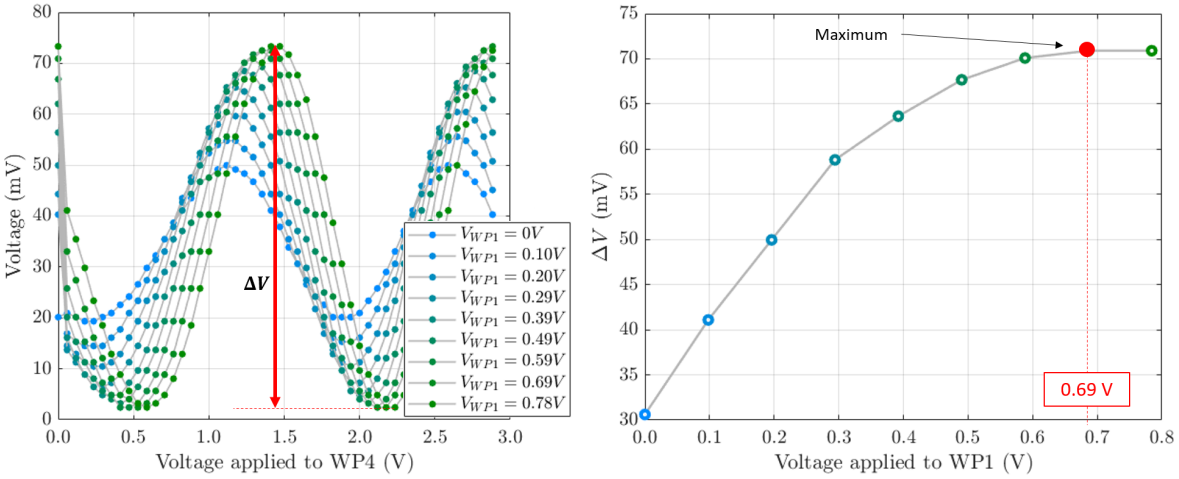

(a) (b)

Figure 4.10: (a) PIN voltages as a function of the voltage applied to the fourth waveplate, considering different voltage values applied to the first waveplate. (b) Plot of ΔV as a function of the voltage applied to the first waveplate.

does not necessarily increase the precision of the output.

4.4 Integration in a QKD System

In order to assess the SOPs generated by the algorithm, we have integrated the proposed technique into a QKD system. The SOP generator was placed at the QKD transmitter, where different SOPs have to be generated according to the employed quantum protocols. The performance of the overall systems was assessed through Quantum Bit Error Rate (*QBER*) measurements.

4.4.1 Description of the QKD System

The QKD system implemented in the laboratory consists of the transmitter, the receiver, and the quantum channel between them, see Fig. 4.11. The transmitter (Alice) is connected to the receiver (Bob) via a quantum channel, used to send the information, and via a classical channel, used to estimate the quality of the communication by calculating the *QBER*.

At the transmitter, two signals are prepared. One is modulated to encode the information in the SOP and the other is used as a reference clock signal. The reference clock signal serves as a trigger clock for the receiver so that the gate of the Single-Photon Detector (SPD)s opens at each rising edge of the clock. The SPDs output a digital signal, where value 1 corresponds to a single-photon detection and the value 0 to no single-photon detection when the gate is open. The proposed SOP generation method explained in Sec. 4.2, is how the main optical signal, used to send the information, is prepared at the transmitter. Both signals, that are generated with different wavelengths, are combined by a Wavelength-Division Multiplexer (WDM) at the output of the transmitter, allowing us to send them through the same optical fiber to the receiver.

At the receiver, apart from opening the gates of the SPDs, the trigger signal also inputs an FPGA in order to process the measurements. The other signal is received by the detection setup, to distinguish between the possible SOPs.

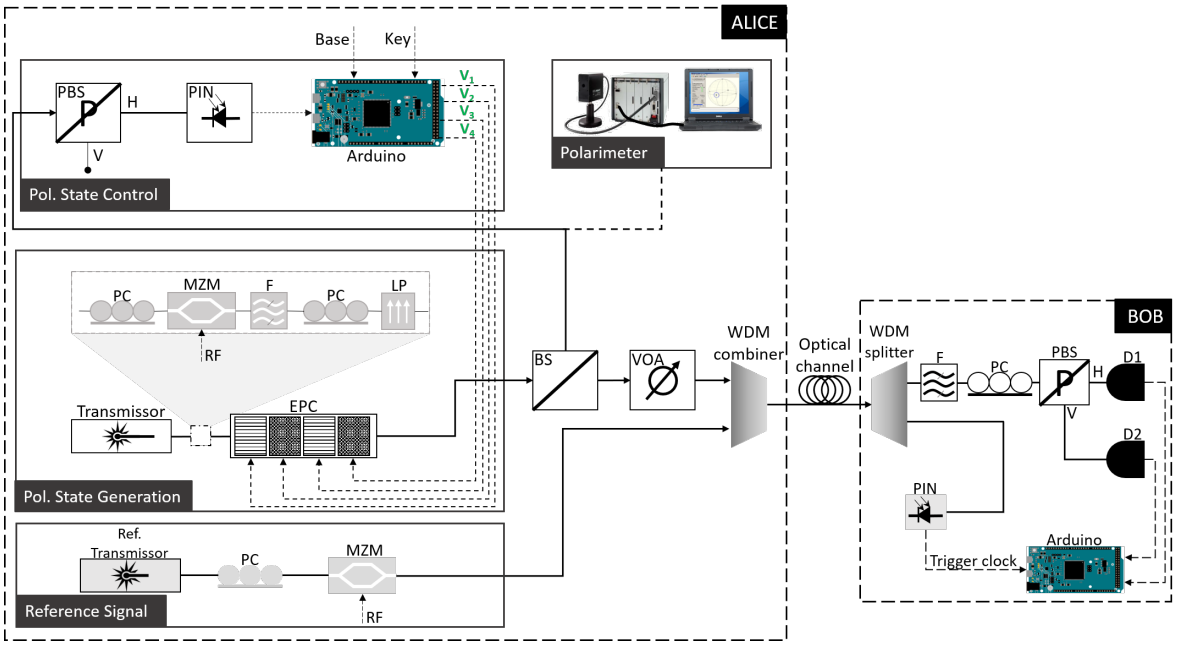

Figure 4.11: Schematic representation of the setup used for *QBER* measurement using two SPDs (D1 and D2). The square denominated Alice represents the transmitter, while the square denominated Bob represents the receiver. Part of the transmitter consists out of the setup proposed for SOP generation. Adapted from [71].

The *QBER* was estimated using the QKD setup shown in Fig. 4.11. Part of the transmitter consists out of the proposed SOP generation system already presented in the previous sections, and corresponds to the first box in Fig. 4.11, denominated “Pol. State Control". The second box is where the signal is prepared, denominated as “Pol. State Generation" in the figure. The combination of the first and the second boxes correspond to the same setup as the one presented in Fig. 4.5, being that part responsible for the SOP generation. The reference signal, mentioned above, is represented in the third box of the transmitter, where an External Cavity Laser (ECL) emits a signal with a wavelength of 1510.00 nm.

The optical signal, carrying the SOP, is attenuated to a quantum level (around 2.8 photons per pulse) by a Variable Optical Attenuator (VOA). The main optical signal and the reference signal are combined and sent through the optical channel. At the receiver, the reference and the quantum signal are wavelength demultiplexed. The reference signal follows to a PIN to set the trigger clock. The quantum signal is guided to an OF that eliminates noise from the reference classical signal, to a manual PC, and then to a PBS that divides horizontally polarized photons from vertically polarized ones. The horizontally polarized photons that arrive at the PBS induce a click on detector D1, while the vertically polarized photons induce a click on detector D2. If the photons are otherwise polarized, for example, specifically with right- or left-hand circular polarizations, the probability of each one of the detectors to click lies at 50%.

For the *QBER* estimation at the receiver, a manual PC is used to align the incoming beam with the PBS horizontal and vertical polarization outputs of the PBS. If the receiver is calibrated with horizontal polarization, only the detector at the horizontally polarized PBS output should detect photons. This way, if horizontally polarized photons are sent by the transmitter, the *QBER* should be around 0%, while if the transmitter sends vertically polarized photons, the *QBER* should be around 100% and, consequently, right-hand circular

or left-hand circular polarized photons should originate a *QBER* of about 50%. On the other hand, if the receiver is calibrated with vertical polarization, the opposite occurs. Meaning that if vertically polarized photons are sent, the *QBER* should be around 0%. The *QBER* was estimated using the method proposed in [20].

4.4.2 QBER Results

QBER measurements were performed for manually and automatically generated SOPs. By a manual SOP generation, it is meant that we measure the SOP with a polarimeter directly connected to the upper arm of the BS, (see Fig. 4.11). By observing the polarimeter, the voltages are chosen until the SOP is guided to the wished polarization point on the Poincaré sphere. The results for the horizontal and vertical SOPs are shown in Fig. 4.12. These measurements were taken for two hours, for each state. Fig. 4.12a shows the *QBER* results when the receiver was aligned with horizontal polarization, while in Fig. 4.12b the receiver was aligned with vertical polarization. The red and blue markers represent the *QBER* for the horizontal and vertical states generated by the algorithm, respectively, and the black continuous line represents the *QBER* obtained for those states with manual operation. For the manually generated SOPs, the transmitter was calibrated at the beginning of the measurements and two hours after (before the state transition), while for the automatically generated SOPs, the transmitter was calibrated only at the beginning of the measurements. Therefore, the estimated *QBER* for the manually generated states, in Fig. 4.12, is not a continuous line.

The raw *QBER*, that has not undergone any post-processing, obtained for the state that was not used for the calibration of the receiver (which corresponds to the vertical state in Fig. 4.12a, and to the horizontal state in Fig. 4.12b) should be around 100%. For a better visualization the *QBER* of Figs. 4.12 and Fig. 4.15, was subjected to post-processing where

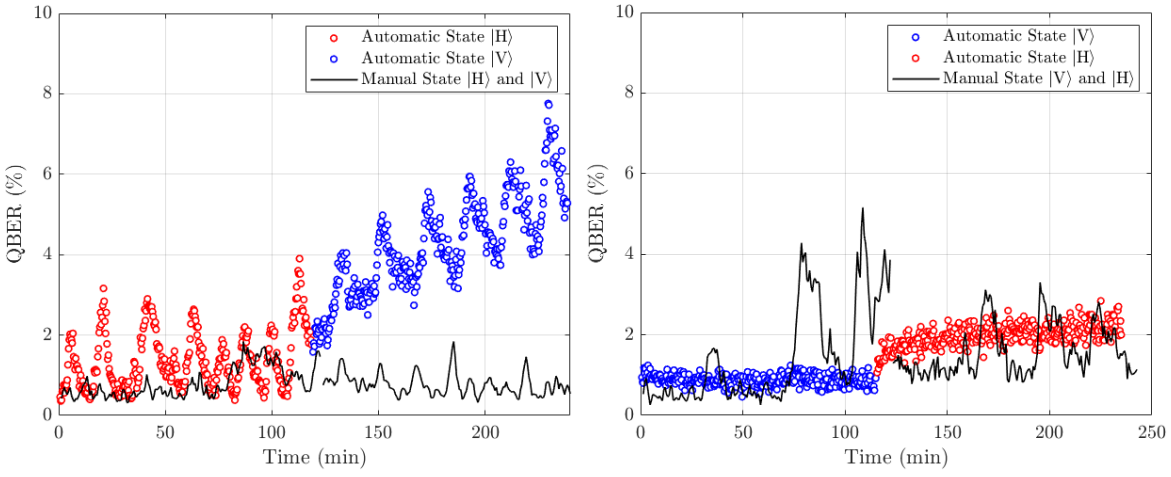

(a) (b)

Figure 4.12: *QBER* estimation obtained for the $|H\rangle$ and $|V\rangle$ states, during two hours each. The red and blue markers represent the automatically generated $|H\rangle$ and $|V\rangle$ states, respectively, while the black line represents the manually generated states. The receiver was manually aligned with: (a) horizontal polarization; (b) vertical polarization. For the manually generated SOPs the transmitter calibrated at the beginning of the measurements and two hours after, while for the automatically generated SOPs the transmitter was calibrated only at the beginning of the measurements.

the QBER of the state not used for the calibration of the receiver is subtracted from 100. For the circular state measurements, the obtained *QBER* is subtracted from 50.

The QBER results of the automatically generated SOPs represented in Fig. 4.12a show periodic oscillations due to environmental perturbations on the quantum channel and due to instabilities of the EPC. These perturbations were weaker when the measurements of Fig. 4.12b were performed. The environmental perturbations are mainly caused by vibrations induced by the air conditioning, working devices, and people moving around. The oscillations in these measurements are not related to the developed algorithm itself, but rather with the environmental perturbations, polarization drift, and EPC instabilities. Similarly, the difference between oscillations of the QBER for the automatically generated SOPs of Fig. 4.12a and Fig. 4.12b does not mean that calibrating the receiver with the vertical state improves the stability. By comparing the *QBER* obtained with the electronic and manual procedures, one can see that the initial value of the manually and automatically generated states is close, corresponding to a similar generation accuracy between both methods.

The next *QBER* results were taken alternating between the horizontal and vertical SOPs. Each state was measured for five minutes. The receiver and the transmitter were only calibrated at the beginning of the measurements. These results are shown in Fig. 4.13. As one can see, the horizontal state *QBER* stays relatively constant, while the vertical state oscillates. The *QBER* values in the middle of the plot, that correspond to values between about 10 and 85% correspond to the transitions between states. As the buffer that registers the values before calculating the *QBER* does not reset between the state transitions, some values are calculated with the *QBER* of the state before and the upcoming state, resulting in *QBER* values in between.

These same measurements were taken, alternating 5 minutes each state, but with more calibrations of the transmitter, as shown in Fig. 4.14a and Fig. 4.14b. Fig. 4.14a shows the *QBER* results with a calibration between each state transition, so every 5 minutes, while in Fig. 4.14b one calibration was made for every two transitions, that is, every 10 minutes. The calibration period of each measurement is shown in Fig. 4.14a and Fig. 4.14b as black vertical lines. As in Fig. 4.13, the *QBER* results of the vertical states are shown near the top of the plot, while the *QBER* results of the horizontal state are at the bottom.

By comparing Fig. 4.13 with Fig. 4.14a and Fig. 4.14b one can see that the *QBER* for the vertical state improved with a higher number of calibrations. However, the state generation

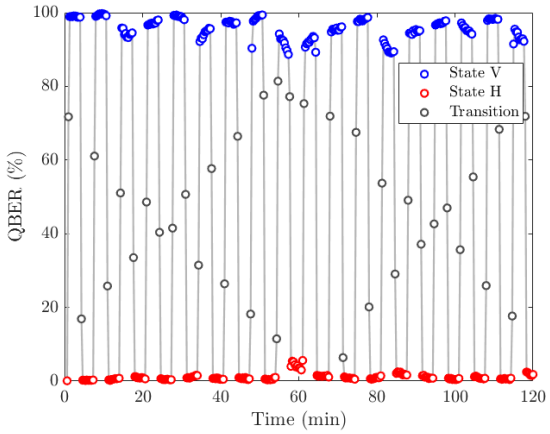

Figure 4.13: QBER obtained for horizontal and vertical states alternating, with one calibration at the beginning of the measurements. Each state was measured for 5 minutes.

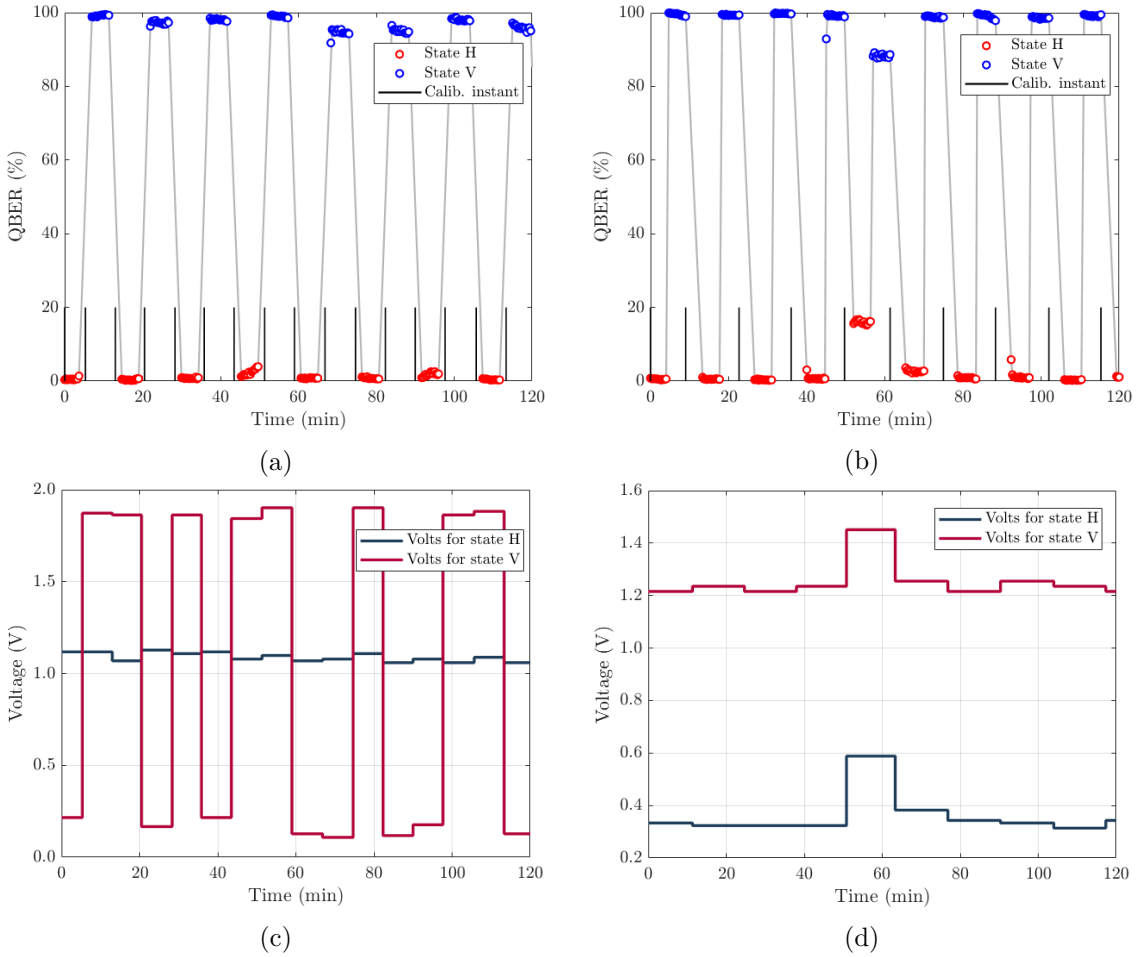

Figure 4.14: (a) *QBER* obtained for horizontal and vertical states, alternating, with calibrations at every state transition. Each state was measured for 5 minutes; (b) *QBER* obtained for $|H\rangle$ and $|V\rangle$ states, alternating, with calibrations at every second state transition. Each state was measured for 5 minutes; (c) Voltages applied for each state in each calibration of Fig. 4.14a; (d) Voltages applied for each state in each calibration of Fig. 4.14b.

seems to be more accurate when a calibration is done only every 10 minutes.

To provide better visualization in Fig. 4.14a and Fig. 4.14b, the calibration points were taken out. With Fig. 4.14c and Fig. 4.14d it is possible to observe which voltages originated the states and how these voltages vary with time. The voltages applied on the fourth waveplate, to generate the horizontal and vertical states are shown in Fig. 4.14c and Fig. 4.14d. In Fig. 4.14c the voltage to generate the horizontal SOP varied between 1.04 and 1.13 V, while the vertical state varied between 0.11 and 1.93. The reason for such a difference in the voltage of the vertical state seems to be that the array of values received from the PIN had two minima. As the values have slight oscillations, the minimum detected by the algorithm is sometimes associated with a value of about 0.11, corresponding to the first minimum, and other times about 1.93, corresponding to the second minimum. The difference between those two values divided by two, i.e. 0.91 V, corresponds to the V_π mentioned above. On the other hand, in Fig. 4.14d, just one minimum and one maximum were detected, causing only slight voltage oscillations, except for one voltage value, for both states. The fifth voltage determined by the algorithm shows a sudden increase compared with the other voltages. This increase is also visible in Fig. 4.14b, where the *QBER* value also shows a noticeable variation. This

outlier might have been caused by an environmental perturbation.

QBER measurements were also performed with the system generating four different SOPs using the proposed method. The results are shown in Fig. 4.15. In this case, the voltages associated with the two circular polarization states were calculated from the voltages determined to generate the two linear states. These measurements were taken for 10 hours and each state was measured during periods of 30 min. An average *QBER* of 2% was achieved. These measurements also show some *QBER* fluctuations. Part of the fluctuations can be due to environmental perturbations, or due to the EPC itself. The continuous voltage change applied to the EPC waveplates might also be a cause for SOP fluctuations. Despite the observed perturbations, results show that the system can be properly calibrated in order to generate four different SOPs to encode the qubits.

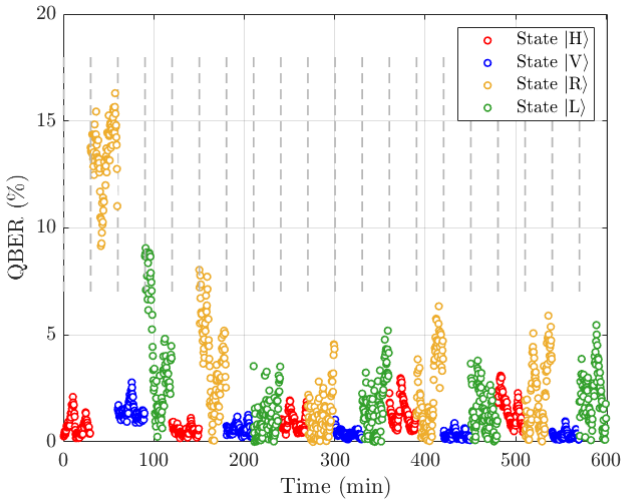

Figure 4.15: *QBER* measurements for the SOPs generated by the proposed algorithm. The four states, $|H\rangle$, $|V\rangle$, $|R\rangle$ and $|L\rangle$ were measured for half an hour each, for a total acquisition time of 10 hours. The receiver was manually aligned on the horizontal SOP.

Chapter 5

Discussion and Conclusions

Quantum Key Distribution (QKD) systems rely on the exchange of single quantum states between two entities. This exchange can be implemented by using single photons as information carriers, where the information itself is encoded in one of the degrees of freedom of the single photons, such as the polarization. Polarization encoding allows for simpler quantum protocols and security proofs, which is a great advantage when envisioning its practical implementation. The practical implementation of polarization-encoded systems lead to diverse studies of the polarization drift during fiber propagation, and it was observed that the State of Polarization (SOP) presents a non-deterministic drift with time, inducing a high Quantum Bit Error Rate (QBER) [22]. Therefore, to enable the deployment of polarization-encoded QKD systems it was necessary to find efficient tools to both characterize and compensate for this random drift [21]. Different methods have been proposed to model and characterize the random polarization drift. Here, we have explored a model that defines the polarization linewidth parameter, Δp, as a single parameter to characterize the polarization evolution in fibers.

In this dissertation, we have carried out a set of experiments, in the laboratory, and on the field to characterize the polarization drift. For the lab measurements, we used two different fiber lengths, 80 and 160 km, and for the field measurements, we explored two sites, an optical loop in the city of Aveiro (with a fiber length of 6.6 km), and an optical link in the city of Lisbon (with a fiber length of 3.1 km). The results show that the Δp obtained in the lab has a much higher value than the one obtained for the field measurements (the 80 and 160 km lab results yield a Δp of $1.7 \times 10^{-6} s^{-1}$, and $5.7 \times 10^{-6} s^{-1}$, respectively, while for the field measurement in Aveiro and Lisbon we obtained a Δp of $8.1 \times 10^{-9} s^{-1}$ and $1.1 \times 10^{-8} s^{-1}$). This means that the polarization drift is much faster in the lab than in the field because the correlation between SOPs drops faster to zero. This, given that the fiber length in the laboratory is much longer than the fiber in the field. This leads to a high decorrelation of the SOP. The difference between the observed Δp values can be explained by the different environmental conditions. In the lab, the experimental setup, including the fiber-optic coils, was placed on a table, thus being more exposed to vibrations and other kinds of perturbations, while the optical link of the field measurements was buried underground, where the environmental conditions are more stable. The random drift of the polarization, even though it is smaller on the field, requires accurate compensation stages. This compensation can be done, for instance, by using Electronic Polarization Controllers (EPC), which is a work still in progress.

In the second part of this dissertation, we presented an algorithm to automatically generate four SOP, to be used in polarization-encoding quantum communication systems. The presented method uses an EPC with four waveplates, allowing us to deterministically

generate four SOPs to be used, for instance, in the Bennett-Brassard 1984 (BB84) protocol. The experimental implementation of the algorithm used an Arduino Due, which ran the algorithm and applied the voltages to the waveplates of the EPC. Several QBER measurements were performed, namely, for the horizontal and vertical polarization states during two hours each state. Alternating measurements were also made, with intermediate calibrations of the transmitter, where the horizontal and vertical polarization states were alternated five in five minutes. Finally, QBER measurements when encoding the horizontal, vertical, right-hand circular, and left-hand circular polarization states were made, with the results showing an average QBER of 2%. The QBER results showed that the proposed method is a viable solution for QKD systems. However, as the polarization drift is a critical issue in fiber-based polarization-encoding quantum communication systems, hereafter, a real-time calibration mechanism should be developed and implemented to stabilize the QBER below the threshold values required by the quantum protocols.

As future work, several aspects can be improved namely the precision of the voltages required to generate the circular SOPs. As mentioned in Sec. 4.2, the circular states are computed by the algorithm and are not determined as the rectilinear states. Therefore, the voltages to generate the circular states are more susceptible to deviations. To overcome this issue, a second path should be included after the Beam Splitter (BS). This branch should have a Quarter Waveplate (QWP) at a 45° angle to transform the circular states to rectilinear states. Then, a Linear Polarizer (LP) or a Polarization Beam Splitter (PBS) should be placed, and then a photodiode, similarly to the setup shown in Fig. 4.5. This way, both rectilinear and circular states can be determined with more precision. Besides, the use of electro-optic polarization controllers would also increase the precision of the SOP generation. The extension of the algorithm proposed in this work for the use of electro-optic polarization controllers would also be an improvement to this system. Another improvement to the presented SOP generation method would be to extend the presented algorithm to generate up to six SOPs, adding the generation of the diagonal SOPs. This way, the developed method can be used in a higher number of quantum protocols. Finally, another aspect to be improved would be to adapt the existing algorithm to compensate for the polarization drift that increases the *QBER*. This adaptation should be a real-time self-compensating algorithm, that ideally, does not need transmission to be interrupted to re-calibrate.

Bibliography

[1] Chi Cheng, Rongxing Lu, Albrecht Petzoldt, and Tsuyoshi Takagi. Securing the internet of things in a quantum world. *IEEE Communications Magazine*, 55(2):116–120, 2017.

[2] Henry Corrigan-Gibbs, Wendy Mu, Dan Boneh, and Bryan Ford. Ensuring high-quality randomness in cryptographic key generation. In *Proceedings of the 2013 ACM SIGSAC conference on Computer & communications security*, pages 685–696. Association for Computing Machinery.

[3] Nicolas Gisin, Grégoire Ribordy, Wolfgang Tittel, and Hugo Zbinden. Quantum cryptography. *Reviews of Modern Physics*, 74(1):145–195, 2002.

[4] Eleni Diamanti, Hoi-Kwong Lo, Bing Qi, and Zhiliang Yuan. Practical challenges in quantum key distribution. *npj Quantum Information*, 2(1):1–12, 2016.

[5] William K. Wootters and Wojciech H. Zurek. A single quantum cannot be cloned. *Nature*, 299(5886):802–803, 1982.

[6] Charles H Bennett and Gilles Brassard. Quantum cryptography: Public key distribution and coin tossing. In *International Conference on Computers, Systems and Signal Processing*, pages 175–179, Bangalore, India, 1984.

[7] Charles H. Bennett and Gilles Brassard. Experimental quantum cryptography: the dawn of a new era for quantum cryptography: the experimental prototype is working. *ACM Sigact News*, 20(4):78–80, 1989.

[8] Abhishek Sharma and Amit Kumar. A survey on quantum key distribution. In *2019 International Conference on Issues and Challenges in Intelligent Computing Techniques (ICICT)*, volume 1, pages 1–4. IEEE, 2019.

[9] Thomas Monz, Daniel Nigg, Esteban A. Martinez, Matthias F. Brandl, Philipp Schindler, Richard Rines, Shannon X. Wang, Isaac L. Chuang, and Rainer Blatt. Realization of a scalable Shor algorithm. *Science*, 351(6277):1068–1070, 2016.

[10] Peter W. Shor. Algorithms for quantum computation: discrete logarithms and factoring. In *Proceedings 35th annual symposium on foundations of computer science*, pages 124–134. IEEE, 1994.

[11] Lov K. Grover. Quantum mechanics helps in searching for a needle in a haystack. *Physical Review Letters*, 79(2):325, 1997.

[12] Wolfgang Tittel. Quantum key distribution breaking limits. *Nature Photonics*, 13(5):310–311, 2019.

[13] Christian Kurtsiefer, P Zarda, Matthus Halder, H Weinfurter, PM Gorman, PR Tapster, and JG Rarity. Quantum cryptography: A step towards global key distribution. *Nature*, 419(6906):450, 2002.

[14] P. C. Sun, Y. Mazurenko, and Y. Fainman. Long-distance frequency-division interferometer for communication and quantum cryptography. *Optics Letters*, 20(9):1062–1064, May 1995.

[15] Thomas Jennewein, Christoph Simon, Gregor Weihs, Harald Weinfurter, and Anton Zeilinger. Quantum cryptography with entangled photons. *Phys. Rev. Lett.*, 84(20):4729–4732, 2000.

[16] N. J. Muga, M. F. Ramos, S. T. Mantey, N. A. Silva, and A. N. Pinto. FPGA-assisted state-of-polarization generation for polarization-encoded optical communications. *IET Optoelectronics*, 14(6):350–355, 2020.

[17] M. Brodsky, N. J. Frigo, M. Boroditsky, and M. Tur. Polarization mode dispersion of installed fibers. *Journal of Lightwave Technology*, 24(12):4584–4599, 2006.

[18] M. F. Ferreira, A. N. Pinto, P. S. Andre, N. J. Muga, J. E. Machado, R. N. Nogueira, S. V. Latas, M. H. Sousa, and J. F. Rocha. Polarization mode dispersion in high-speed optical communication systems. *Fiber and Integrated Optics*, 24(3-4):261–285, 2005.

[19] Yu-Yang Ding, Hua Chen, Shuang Wang, De-Yong He, Zhen-Qiang Yin, Wei Chen, Zheng Zhou, Guang-Can Guo, and Zheng-Fu Han. Polarization variations in installed fibers and their influence on quantum key distribution systems. *Optics Express*, 25(22):27923–27936, 2017.

[20] Á. Almeida, N. Muga, N. Silva, J. Prata, P. André, and A. Pinto. Continuous control of random polarization rotations for quantum communications. *Journal of Lightwave Technology*, 34(16):3914–3922, 2016.

[21] M. Ramos, N. Muga, and A. Pinto. Reversal operator to compensate random drifts in polarization-encoded quantum communications. *Optics Express*, 28(4):5035–5049, 2020.

[22] N. J. Muga, M. Ferreira, and A. N. Pinto. QBER estimation in QKD systems with polarization encoding. *Journal of Lightwave Technology*, 29(3):355–361, 2011.

[23] Heasin Ko, Byung-Seok Choi, Joong-Seon Choe, Kap-Joong Kim, Jong-Hoi Kim, and Chun Ju Youn. High-speed and high-performance polarization-based quantum key distribution system without side channel effects caused by multiple lasers. *Photonics Research*, 6(3):214–219, 2018.

[24] Yang Li, Yu-Huai Li, Hong-Bo Xie, Zheng-Ping Li, Xiao Jiang, Wen-Qi Cai, Ji-Gang Ren, Juan Yin, Sheng-Kai Liao, and Cheng-Zhi Peng. High-speed robust polarization modulation for quantum key distribution. *Optics Letters*, 44(21):5262–5265, 2019.

[25] Zhizhong Yan, Evan Meyer-Scott, Jean-Philippe Bourgoin, Brendon L. Higgins, Nikolay Gigov, Allison MacDonald, Hannes Hübel, and Thomas Jennewein. Novel high-speed polarization source for decoy-state BB84 quantum key distribution over free space and satellite links. *Journal of Lightwave Technology*, 31(9):1399–1408, 2013.

[26] Cristian B. Czegledi, Magnus Karlsson, Erik Agrell, and Pontus Johannisson. Polarization drift channel model for coherent fibre-optic systems. *Scientific reports*, 6(1):1–11, 2016.

[27] Dennis H Goldstein. *Polarized light*. CRC press, 2016.

[28] Rasheed M. A. Azzam and Nicholas Mitchell Bashara. Ellipsometry and polarized light. *Physics Today*, 31(11):72, 1978.

[29] Edward Collett. Field guide to polarization. Spie Bellingham, WA, 2005.

[30] Vincenzo Dámbrosio, Filippo Cardano, Ebrahim Karimi, Eleonora Nagali, Enrico Santamato, Lorenzo Marrucci, and Fabio Sciarrino. Test of mutually unbiased bases for six-dimensional photonic quantum systems. *Scientific reports*, 3(2726), 2013.

[31] Jay N Damask. *Polarization Optics in Telecommunications*, volume 101. Springer Science & Business Media, 2004.

[32] George Gabriel Stokes. *On the Effect of the Internal Friction of Fluids on the Motion of Pendulums*, volume 3, pages 1–10. Cambridge University Press, 2009.

[33] William H McMaster. Polarization and the Stokes parameters. *American Journal of Physics*, 22(6):351–362, 1954.

[34] Nelson Muga. Dispersão dos modos de polarização em fibras Ópticas. Master's thesis, Universidade de Aveiro, 2006.

[35] Nelson Muga. *Polarization Effects in Fiber-Optic Communication Systems*. PhD thesis, Universidade de Aveiro, 2011.

[36] J. P. Gordon and H. Kogelnik. PMD fundamentals: Polarization mode dispersion in optical fibers. 97(9):4541–4550, 2000.

[37] Sharmini Pillay, Abdul Mirza, and Francesco R. Petruccione. Towards polarisation-encoded quantum key distribution in optical fibre networks. *South African Journal of Science*, 111(7-8):1–6, 2015.

[38] H. P. Robertson. The uncertainty principle. *Physical Review*, 34(1):163–164, 1929.

[39] Govind Agrawal. *Nonlinear fiber optics*. Quantum electronics–principles and applications. Elsevier and Academic Press, 4th edition, 2007.

[40] Cristian B. Czegledi. *Modeling and Tracking of Stochastic Polarization Drifts in Fiber-optic Systems*. PhD thesis, Chalmers University of Technology, 2016.

[41] F. Heismann and Ka Tokuda. Polarization-independent electro-optic depolarizer. *Optics Letters*, 20(9):1008–1010, 1995.

[42] Seb Savory. Digital filters for coherent optical receivers. *Optics Express*, 16(2):804–817, 2008.

[43] N. J. Muga and A. N. Pinto. Adaptive 3D Stokes space based polarization demultiplexing algorithm. *Journal of Lightwave Technology*, 32(19):3290–3298, 2014.

[44] Hadrien Louchet, Konstantin Kuzmin, and Andre Richter. Joint carrier-phase and polarization rotation recovery for arbitrary signal constellations. *Photonics Technology Letters, IEEE*, 26(9):922–924, 2014.

[45] Ling Liu, Zhenning Tao, Weizhen Yan, Shoichiro Oda, Takeshi Hoshida, and Jens C. Rasmussen. Initial tap setup of constant modulus algorithm for polarization de-multiplexing in optical coherent receivers. In *Optical Fiber Communication Conference and National Fiber Optic Engineers Conference*. OSA, 2009.

[46] Kazuro Kikuchi. Polarization-demultiplexing algorithm in the digital coherent receiver. In *2008 Digest of the IEEE/LEOS Summer Topical Meetings*, pages 101–102. IEEE, 2008.

[47] Ioannis Roudas, Athanasios Vgenis, Constantinos Petrou, Dimitris Toumpakaris, Jason Hurley, Michael Sauer, John Downie, Yihong Mauro, and Srikanth Raghavan. Optimal polarization demultiplexing for coherent optical communications systems. *Journal of Lightwave Technology*, 28(7):1121–1134, 2010.

[48] Pontus Johannisson, Henk Wymeersch, Martin Sjödin, A. Serdar Tan, Erik Agrell, Peter Andrekson, and Magnus Karlsson. Convergence comparison of the cma and ica for blind polarization demultiplexing. *Journal of Optical Communications and Networking*, 3(6):493–501, 2011.

[49] C.D. Poole and R.E. Wagner. Phenomenological approach to polarization dispersion in long single-mode fibers. *Electronics Letters*, 22(19):1029 – 1030, 1986.

[50] George Soliman, M. Reimer, and David Yevick. Measurement and simulation of polarization transients in dispersion compensation modules. *Journal of the Optical Society of America. A, Optics, Image Science, and Vision*, 27(12):2532–2541, 2010.

[51] Eugene Hecht et al. *Optics*, volume 4. Addison Wesley San Francisco, 2002.

[52] Mário Ferreira. *Óptica e Fotónica*. Lidel, 2003.

[53] Russell A. Chipman, Wai Sze Tiffany Lam, and Garam Young. *Polarized light and optical systems*. CRC press, 2018.

[54] Thorlabs Instrumentation. *Polarization Analyzing System - Operation Manual*, 2008.

[55] Max Born and Emil Wolf. *Principles of optics: electromagnetic theory of propagation, interference and diffraction of light*. Elsevier, 6th edition, 2013.

[56] Beth Schaefer, Edward Collett, Robert Smyth, Daniel Barrett, and Beth Fraher. Measuring the Stokes polarization parameters. *American Journal of Physics*, 75(2):163–168, 2007.

[57] John R. Barry, Edward A. Lee, and David G. Messerschmitt. *Digital communication*. Springer Science & Business Media, 2012.

[58] M. K. Barnoski and S. M. Jensen. Fiber waveguides: a novel technique for investigating attenuation characteristics. *Applied Optics*, 15(9):2112–2115, Sep 1976.

[59] EXFO. *Users Guide - AXS-100 Series OTDR*, 2010.

[60] M Kubota, T Oohara, K Furuya, and Y Suematsu. Electro-optical polarisation control on single-mode optical fibres. *Electronics letters*, 16(15):573–573, 1980.

[61] T. Imai, K. Nosu, and H. Yamaguchi. Optical polarisation control utilising an optical heterodyne detection scheme. *Electronics letters*, 21(2):52–53, 1985.

[62] R. Ulrich. Polarization stabilization on single-mode fiber. *Applied Physics Letters*, 35(11):840–842, 1979.

[63] T. Okoshi, Y. H. Cheng, and K. Kikuchi. New polarisation-control scheme for optical heterodyne receiver using two faraday rotators. *Electronics Letters*, 21(18):787–788, 1985.

[64] H. C. Lefevre. Single-mode fibre fractional wave devices and polarisation controllers. *Electronics Letters*, 16(20):778–780, 1980.

[65] N. J. Muga, A. N. Pinto, M. F. S. Ferreira, and José R. Ferreira da Rocha. Uniform polarization scattering with fiber-coil-based polarization controllers. *Journal of Lightwave Technology*, 24(11):3932–3943, 2006.

[66] P Granestrand and L Thylen. Active stabilisation of polarisation on a single-mode fibre. *Electronics Letters*, 20(9):365–366, 1984.

[67] Steve Yao. Polarization in fiber systems: Squeezing out more bandwidth. *The Photonics Handbook*, page 1, 2003.

[68] *Operation Manual - Miniature Multi-Channel Piezoelectric Actuator Driver Card / Integrated PolaRITE III Polarization Controller*, 2018.

[69] J. Larry Pezzaniti and Russell A. Chipman. Angular dependence of polarizing beam-splitter cubes. *Applied Optics*, 33(10):1916–1929, 1994.

[70] N. J. Muga, M. F. Ramos, S. T. Mantey, N. A. Silva, and A. N. Pinto. Deterministic state-of-polarization generation for polarization-encoded optical communications. In *Microwave and Optoelectronics Conference (IMOC) SBMO/IEEE MTT-S International*, Aveiro, November 2019.

[71] S. T. Mantey, M. F. Ramos, N. A. Silva, A. N. Pinto, and N. J. Muga. Algorithm for state-of-polarization generation in polarization-encoding quantum key distribution. Accepted for presentation in the Telecoms Conference (ConfTELE), 2021.